Title
Baroclinic instability of axially symmetric flow over sloping bathymetry

Authors
Solodoch, Aviv
Stewart, Andrew L
McWilliams, James C

Publication Date
2016-07-25

DOI
10.1017/jfm.2016.376

Peer reviewed

Baroclinic instability of axially-symmetric flow over sloping bathymetry

Aviv Solodoch[1]†, Andrew L. Stewart[1] and James C. McWilliams[1]

[1]Department of Atmospheric and Oceanic Sciences, University of California, Los Angeles, CA 90095, USA

(Received xx; revised xx; accepted xx)

Observations and models of deep ocean boundary currents show that they exhibit complex variability, instabilities and eddy shedding, particularly over continental slopes that curve horizontally, for example around coastal peninsulas. In this article the authors investigate the source of this variability by characterizing the properties of baroclinic instability in mean flows over horizontally curved bottom slopes. The classical 2-layer quasi-geostrophic solution for linear baroclinic instability over sloping bottom topography is extended to the case of azimuthal mean flow in an annular channel. To facilitate comparison with the classical straight channel instability problem of uniform mean flow, the authors focus on comparatively simple flows in an annulus, namely uniform azimuthal velocity and solid-body rotation. Baroclinic instability in solid-body rotation flow is analytically analogous to the instability in uniform straight channel flow due to several identical properties of the mean flow, including vanishing strain rate and vorticity gradient. The instability of uniform azimuthal flow is numerically similar to straight channel flow instability as long as the mean barotropic azimuthal velocity is zero. Nonzero barotropic flow generally suppresses the instability via horizontal curvature-induced strain and Reynolds stresses work. An exception occurs when the ratio of the bathymetric to isopycnal slopes is close to (positive) one, as is often observed in the ocean, in which case the instability is enhanced. A non-vanishing mean barotropic flow component also results in a larger number of growing eigenmodes and in increased non-normal growth. The implications of these findings for variability in deep western boundary currents are discussed.

1. Introduction

Baroclinic instability is one of the main energy conversion processes to and from the mesoscale in the ocean (McWilliams 2008). The baroclinic source of energy, available potential energy due to tilting of isopycnals (constant density surfaces), is ubiquitous. Studies based on high-resolution altimetry (Chelton *et al.* 2011) reveal that virtually all areas of the world's oceans are sources of mesoscale eddies, and therefore may be baroclinically unstable. A few of the many roles mesoscale eddies play in the ocean are: supporting the forward and inverse turbulent energy cascades, relaxing isopycnal slopes and thus restratifying the ocean, vertical transfer of momentum via the eddy form stress and transport, and ventilation and subdaction of tracers (McWilliams 2008; Dong *et al.* 2014).

Baroclinic eddy variability peaks in the ocean near strong persistent currents (Chelton *et al.* 2011), such as large boundary currents (e.g., the Gulf Stream). The task of measuring and characterizing eddy generation mechanisms is more challenging for deep

† Email address for correspondence: asolodoch@atmos.ucla.edu

(sub-surface intensified) boundary currents, since they are much less amenable to remote sensing, and since even after decades of oceanographic expeditions, in situ measurements are quite sparse. A prominent example is the variability associated with the Deep Western Boundary Current (DWBC) in the Grand Banks (GB) area, where eddy shedding and interior flow pathways are prevalent, as observational campaigns using deep Lagrangian floats have revealed (Lavender *et al.* 2000, 2005; Bower *et al.* 2009).

The data presented in Bower *et al.* (2009) suggest that the horizontally curving slopes around the GB and Flemish Cap (FC) are associated with increased eddy generation relative to less curved portions. The curvature, convex or concave, we refer to is of isobaths, horizontal lines of constant bottom depth. Thus "underwater capes" such as GBs and FC, are convex, while the area between them is concave. Arguably, the data also visually suggest greater eddy generation at convex sections of the continental slope than at concave sections. Their figure 1 suggests that nearly all floats cross the 4000 meter isobath off-shore after drifting south to FC (where the continental slope is convex), most of which do not return to the DWBC further downstream. The few floats that remain shoreward of the 4000 meter isobath, do not drift significantly further off-shore until they reach the next convex segment, the GB. In the GB area more floats are shed from the continental slope and cross the 4000 meter isobath. Lavender *et al.* (2005) found similar loss of floats to the interior ocean at the vicinity of FC, as well as a maximum in eddy kinetic energy there. Since the floats are generally drifting with the (baroclinic) DWBC, these findings raise the possibility that the influence of coastal curvature on baroclinic instability could explain the localization of eddy generation around FC and GB. There are many dynamically similar examples of boundary currents leaking around convex continental slopes, such as the Mediterranean Overflow Water, which sheds Submesoscale-Coherent Vortices as it propagates around the Iberian peninsula (McDowell & Rossby 1978; McWilliams 1985; Bower *et al.* 1997). The California Undercurrent also sheds submesoscale eddies at convex bends, for example at the mouth of Monterey Bay (Stegmann & Schwing 2007; Molemaker *et al.* 2015).

To study the influence of horizontal curvature in a controlled setting, we employ a model of minimal complexity that admits baroclinic instability, a 2-layer quasi-geostrophic (QG) model, in an annular channel. This model is a geometric variant of the straight-channel 2-layer QG model presented in Pedlosky (1964). The case of linear baroclinic instability in horizontally-uniform QG flow over a flat bottom was solved by Phillips (1951) with 2 vertical layers and by Eady (1949) with a continuous vertical coordinate. Blumsack & Gierasch (1972) extended the Eady model to include a sloping bottom boundary. Mechoso (1980) similarly extended the Phillips model, and systematically investigated the influence of a sloping bottom boundary in both models. Pedlosky (1964) derived integral stability constraints for instability, for a more general family of straight channel flows over sloping bathymetry. Multiple investigators found that linear 2-layer baroclinic instability models compared well with observed variability in boundary currents over continental slopes in various regions, including the Denmark Straight Overflow (Smith 1976), the Norwegian Current (Mysak & Schott 1977), and the Färoe-Shetland flow (Sherwin *et al.* 2006). Phase speeds and wavelengths were within $\sim 30\%$ of observed values, and eigenmode structures were qualitatively similar to those derived from observations. Other authors have attempted to incorporate this theory into eddy parameterizations over continental slopes (Stipa 2004*b*; Isachsen 2011).

Choboter & Swaters (2000) used a non-QG asymptotic derivation to analyze the baroclinic instability of a double-frontal dense water layer over sloping topography in an annulus. Their explicit solutions are for a relatively narrow (1.5 Rossby radii apart at the bottom) coupled front on the bottom of an otherwise stationary fluid,

whereas we investigate wider and more horizontally-uniform 2-layer flows here. Since we model wider currents, we use the approximation that isopycnals do not intersect the bathymetry, consistent with the QG approximation. In addition, our focus here is deducing the influence of horizontal curvature on the instability, whereas Choboter & Swaters (2000) aimed to compare an existing theory for rectilinear bottom-trapped flow against laboratory experiments in a rotating tank.

A key measure of the effect of bathymetry on baroclinic instability is the ratio of the bathymetric slope to the mean isopycnal slope (hereafter δ, see also figure 1, and §2.4). Blumsack & Gierasch (1972) found that the wavelength of the most rapidly growing mode was lower (higher) for negative (positive) δ, compared to the wavelength at $\delta = 0$, and that the mean flow was stable to all disturbances for $\delta > 1$. Mechoso (1980) reported the same result for the analogous case in a 2-layer model. Isachsen (2011) used δ to characterize the topographic regime in both Eady model calculations and in nonlinear three-dimensional simulations. We similarly use δ throughout this paper to quantify the influence of the topographic slope.

The outline of this paper is as follows. In §2 we present the model, and in §3 we derive integral theorems that constrain the growth rates and phase speeds of unstable waves. In §4 we apply the model to investigate instability of solid-body rotation over parabolic bathymetry, and establish a close analogy with straight channel uniform flow over linear bathymetry (Appendix B, hereafter uniform rectilinear flow). In §5 we similarly, and in more detail, investigate instability of uniform azimuthal flow in an annulus over linear bathymetry. In §6 we discuss the essential factors, independent of channel geometry, that make uniform rectilinear flow and solid body rotation similar and uniform azimuthal flow quite different. We briefly discuss a few other experiments in support of the generality of these factors and their influence on baroclinic instability. In §7 we discuss our results and their relevance to the stability of oceanic boundary currents.

2. Linear model of baroclinic growth in an annular channel

A schematic drawing of the domain and model is shown in figure 1. We model a horizontally-curved continental slope as an annular channel, in which the walls represent the shoreward and offshore extents of a baroclinic slope-trapped current. We model the mean current as a 2-layer axisymmetric azimuthal flow, a minimal discrete approximation to a continuous density stratification. We prescribe different geostrophic mean velocities in each layer, creating a vertical shear and thus allowing the possibility of baroclinic instability. The vertical axis is denoted by z, and the reference frame is assumed to revolve around that axis to imitate the earth's rotation (§2.1).

2.1. *Quasi-geostrophic model equations in cylindrical coordinates*

In this section we present the QG potential vorticity (PV) and energy equations for axially symmetric mean flow and bathymetry. Quasigeostrophy is an approximation to fluid flow in a rotating reference frame, which is often a good approximation for synoptic scale oceanic flows (oceanic mesoscale), i.e., with characteristic lengthscales comparable with the Rossby radius of deformation, defined below (Pedlosky 1987). The necessarily small parameter in the approximation is the Rossby number $\mathrm{Ro} = U/fX \ll 1$, where f is the Coriolis parameter, U the velocity scale and X the horizontal lengthscale. In these cases the Coriolis force approximately balances the pressure gradient, and to first order in Ro, the evolution of the flow field is given by the QG PV equations. The QG approximation also requires the bathymetry and isopycnals to exhibit small variations relative to their respective domain-wide averages. While these conditions

are not necessarily satisfied over continental slopes, previous studies suggest that QG captures the essential features of large-scale flows over topographic steepnesses typical of the ocean's continental slopes (Williams *et al.* 2010; Stewart *et al.* 2011, 2014; Poulin *et al.* 2014; Stern *et al.* 2015).

We use the f-plane approximation (Pedlosky 1987), in which the reference frame revolves around the vertical axis with the same rate everywhere in the domain, neglecting the effect of the Earth's curvature on the Coriolis acceleration. This isolates the effect of continental slope curvature, and thereby simplifies our analysis. This is partially justified by the fact that, dynamically, a topographic gradient induces a similar dynamical effect on rotating flow as does the latitudinal gradient of the rotation rate. This so-called topographic β effect is usually much larger than the planetary β effect in the local dynamics of slope-trapped currents.

We write the 2-layer QG PV equations (Pedlosky 1964) in cylindrical coordinates,

$$\left[\frac{\partial}{\partial\tilde{t}}+\tilde{u}_{1r}\frac{\partial}{\partial\tilde{r}}+\frac{\tilde{u}_{1\phi}}{\tilde{r}}\frac{\partial}{\partial\tilde{\phi}}\right]\left[\tilde{\nabla}^2\tilde{\psi}_1-\frac{1}{L_1^2}(\tilde{\psi}_1-\tilde{\psi}_2)\right]=0, \tag{2.1a}$$

$$\left[\frac{\partial}{\partial\tilde{t}}+\tilde{u}_{2r}\frac{\partial}{\partial\tilde{r}}+\frac{\tilde{u}_{2\phi}}{\tilde{r}}\frac{\partial}{\partial\tilde{\phi}}\right]\left[\tilde{\nabla}^2\tilde{\psi}_2-\frac{1}{L_2^2}\left(\tilde{\psi}_2-\tilde{\psi}_1-\frac{g'}{f_0}\tilde{\eta}_b\right)\right]=0. \tag{2.1b}$$

The upper and lower layer variables are denoted by the subscripts 1 and 2 respectively. Tildes are used since we will later nondimensionalize the equations and use variables without tildes. The annular channel interior and exterior radii are denoted by $\tilde{R}_i$ and $\tilde{R}_e$ respectively. The radial ($\tilde{r}$) and azimuthal ($\tilde{\phi}$) velocity components are related to the streamfunction $\tilde{\psi}_j$ by $(\tilde{u}_{jr},\ \tilde{u}_{j\phi})=\left(-\tilde{r}^{-1}\partial\tilde{\psi}_j/\partial\tilde{\phi},\ \partial\tilde{\psi}_j/\partial\tilde{r}\right)$. Vorticity $\tilde{\zeta}_j$ is related to the streamfunction by $\tilde{\zeta}_j=\tilde{\nabla}^2\tilde{\psi}_j$. Other parameters include the gravitational acceleration g, the density ρ_j, the reduced gravity $g'=g\frac{\rho_2-\rho_1}{\rho_1}$, the average layer thicknesses H_j, the reference Coriolis parameter f_0, the Rossby radii of deformation $L_j=\sqrt{g'H_j}/f_0$, and the bottom elevation $\tilde{\eta}_b(\tilde{r})$. For boundary conditions, we require that there be no flow normal to the inner and outer walls, $\partial\tilde{\psi}_j/\partial\tilde{\phi}=0\ |_{\tilde{r}=\tilde{R}_i,\tilde{R}_e}$.

To study the instability of currents flowing parallel to the bathymetric isobaths, we assume a geostrophic, axially-symmetric, azimuthal mean flow $\tilde{U}_{j\phi}(\tilde{r})=\partial\overline{\tilde{\psi}}_j/\partial\tilde{r}$. This is an exact steady solution of (2.1a)–(2.1b). We partition the streamfunction into mean and perturbation components, $\overline{\tilde{\psi}}_j$ and $\tilde{\psi}'_j$ respectively. Linearizing the QG PV equations (2.1a)–(2.1b) yields a linear system of equations for the perturbation streamfunctions,

$$\left[\frac{\partial}{\partial\tilde{t}}+\frac{\tilde{U}_{1\phi}}{\tilde{r}}\frac{\partial}{\partial\tilde{\phi}}\right]\left[\tilde{\nabla}^2\tilde{\psi}'_1-\frac{1}{L_1^2}(\tilde{\psi}'_1-\tilde{\psi}'_2)\right]-\frac{1}{\tilde{r}}\frac{\partial\tilde{\psi}'_1}{\partial\tilde{\phi}}\frac{\partial\tilde{Q}_1}{\partial\tilde{r}}=0, \tag{2.2a}$$

$$\left[\frac{\partial}{\partial\tilde{t}}+\frac{\tilde{U}_{2\phi}}{\tilde{r}}\frac{\partial}{\partial\tilde{\phi}}\right]\left[\tilde{\nabla}^2\tilde{\psi}'_2-\frac{1}{L_2^2}(\tilde{\psi}'_2-\tilde{\psi}'_1)\right]-\frac{1}{\tilde{r}}\frac{\partial\tilde{\psi}'_2}{\partial\tilde{\phi}}\frac{\partial\tilde{Q}_2}{\partial\tilde{r}}=0, \tag{2.2b}$$

$$\tilde{Q}_j=\tilde{\nabla}^2\overline{\tilde{\psi}_j}-\frac{1}{L_j^2}\left[(-1)^j\left(\overline{\tilde{\psi}_2}-\overline{\tilde{\psi}_1}\right)-\Delta_{j2}\frac{g'}{f_0}\tilde{\eta}_b\right]. \tag{2.2c}$$

Here $\Delta_{j2}=0,1$ for $j=1,2$ respectively.

The model describes a concave (convex) continental slope is if $\tilde{\eta}_b(\tilde{r})$ is monotonically increasing (decreasing) with radius. A given convex (concave) along-slope flow can be transformed to the analogous concave (convex) along-slope flow by a radial reflection $P(\tilde{r}-\tilde{R}_i)\to P(\tilde{R}_e-\tilde{r})$, for any scalar radial property $P(\tilde{r}-\tilde{R}_i)$ of the mean state, such as bathymetry $\tilde{\eta}_b(r)$ or isopycnal profile $\tilde{Z}_I(\tilde{r})$.

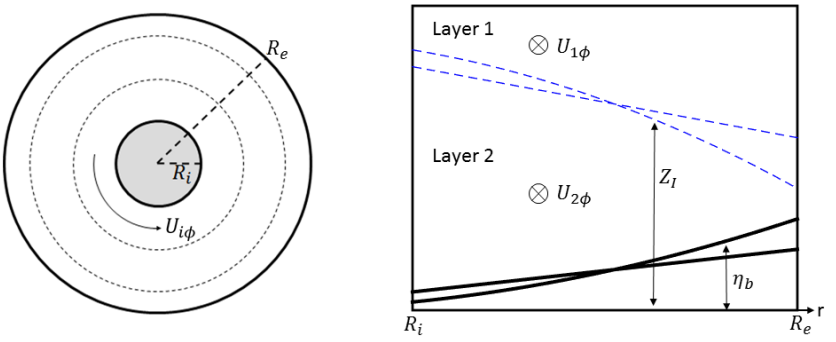

FIGURE 1. Schematic drawing of the domain boundaries, bathymetry and mean circulation. (left) Top-down view of the annular channel, with dashed lines representing isobaths or mean streamlines. (right) Along-slope view of the mean flow configuration. The dashed line represents the isopycnal profile $z = Z_I(r)$, the interface between the two fluid layers. Two particular bathymetry ($\eta_b(r)$) and isopycnal profile pairs are plotted here, linear and parabolic in r, corresponding to uniform azimuthal flow and solid body rotation, respectively. The isopycnal and bathymetric profiles for uniform rectilinear flow are identical to those of uniform azimuthal flow, i.e., linear in the cross-channel coordinate. A rigid lid is assumed, consistent with stratified quasi-geostrophy. The δ parameter, i.e., ratio of bathymetric to isopycnal slopes, is negative in both specific cases displayed here, although both signs are considered in this study.

The baroclinic growth rate in uniform rectilinear flow (Mechoso 1980) peaks close to the wavenumber corresponding to the first baroclinic Rossby radius of deformation. Therefore we non-dimensionalize the equations by scaling $\tilde{r} \sim L$, where

$$L = \sqrt{\frac{g' H_1 H_2}{f_0^2 \, (H_1 + H_2)}}. \tag{2.3}$$

We denote the velocity scale (to be specified later) by U. The non-dimensional variables are defined by

$$t = (L/U)^{-1}\tilde{t}, \quad U_{j\phi} = U^{-1}\tilde{U}_{j\phi}, \quad \eta_b = (UL f_0/g')^{-1}\tilde{\eta}_b, \quad r = L^{-1}\tilde{r}. \tag{2.4}$$

For notational convenience we also define $F_j = L^2/L_j^2 = 1 - H_j/(H_1 + H_2)$, which measures the fraction of the total depth that is not occupied by layer j. Although F_1 and F_2 are not independent, we shall keep both parameters to preserve some symmetry in the presentation of the equations.

2.2. *Method of solution*

In what follows we drop the prime notation from the perturbation streamfunction for ease of presentation. The eigenvalue problem is derived by decomposing the perturbation streamfunction into normal azimuthal and temporal modes,

$$\psi_j = \mathrm{Re}\left\{\Psi_j(r)\exp(i(m\phi - \sigma t))\right\}. \tag{2.5}$$

The notation Re {} indicates the real part of the expression in the curly braces, and $i \equiv \sqrt{-1}$. The azimuthal wavenumber is denoted as m, and σ is the nondimensional complex frequency (dimensional $\tilde{\sigma}$ scales like (U/L) by (2.4)). The real and imaginary parts of

σ are the frequency and the growth rate, respectively. The no-normal flow boundary condition (stated above) simplifies to $\Psi_j|_{r=R_i,R_e} = 0$. Writing $\nabla_r^2 = (\frac{\partial}{\partial r} + \frac{1}{r})\frac{\partial}{\partial r}$, the linear vorticity equations (2.2a)–(2.2b) may be simplified as

$$\left[\frac{U_{1\phi}}{r}m - \sigma\right]\left[\nabla_r^2\Psi_1 - \frac{m^2}{r^2}\Psi_1 - F_1(\Psi_1 - \Psi_2)\right] - \frac{m}{r}\Psi_1\frac{\partial Q_1}{\partial r} = 0, \tag{2.6a}$$

$$\left[\frac{U_{2\phi}}{r}m - \sigma\right]\left[\nabla_r^2\Psi_2 - \frac{m^2}{r^2}\Psi_2 - F_2(\Psi_2 - \Psi_1)\right] - \frac{m}{r}\Psi_2\frac{\partial Q_2}{\partial r} = 0, \tag{2.6b}$$

$$\frac{\partial Q_j}{\partial r} = \frac{\partial}{\partial r}\left(\frac{\partial}{\partial r} + \frac{1}{r}\right)U_{j\phi} - F_j(-1)^j\left[(U_{2\phi} - U_{1\phi}) - \Delta_{j2}\frac{\partial \eta_b}{\partial r}\right]. \tag{2.6c}$$

In most cases presented below we solve the eigenproblem posed by (2.6a)–(2.6c) numerically. We discretize equations (2.6a)–(2.6b) using second-order centered finite differences and solve the resulting matrix eigenvalue problem using the "eig" function in Matlab, which uses the QZ algorithm (Moler & Stewart 1973). The grid resolution is $dr = 0.025$, giving 40 grid points per Rossby radii, thus resolving well the spatial scales normally associated with QG dynamics. Verification of the numerical setup including convergence tests and comparison with some analytic results are presented in Appendix A. The standard experiment parameters are: $F_1 = F_2 = 1/2$, $R_i = 3$, $R_e = 10$. The chosen channel width ($R_e - R_i$) is motivated by the widths of deep western boundary currents, which are typically at least a few Rossby radii (Xu *et al.* 2015; Stommel & Arons 1972). Similar bathymetric curvature radii (in the range of $3-10$ Rossby radii) are found around the Grand Banks and Flemish Cap. Other parameter ranges and sensitivity tests are discussed in Appendix A.

2.3. *Energy equation*

To study the modes of energy conversion from the mean state to perturbations, we derive the volume-integrated energy equation. The general method is standard (Pedlosky 1987): multiplying equations (2.2a) and (2.2b) by $D_1\psi_1$ and $D_2\psi_2$ respectively, adding the two resulting equations together, integrating in the entire domain, and using several integrations by parts and the no-normal flow boundary conditions. We defined the relative layer thicknesses D_i, by $D_1 = F_2 = H_1/(H_1 + H_2)$ and $D_2 = F_1 = H_2/(H_1 + H_2)$. In addition, one line integral over the domain boundaries, $\sum_{j=1}^{2} D_j \oint \psi_j' \frac{\partial^2}{\partial t \partial n}\psi_j' ds$ (where n is the normal to the boundary), is required to vanish (McWilliams, 1977, specifically equation 13), for consistency with the analogous asymptotic expansion (in Rossby number) of the Primitive Equations energy balance. The derived energy equation in non-dimensional variables is

$$\frac{\partial}{\partial t}E = \frac{\partial}{\partial t}\left\{\sum_{j=1}^{2} EKE_j + EPE\right\} = \sum_{j=1}^{2} RS_j + PEC, \tag{2.7a}$$

$$EKE_j = \frac{1}{2}D_j \iint (\nabla\psi_j)^2 \, r \,\mathrm{d}r \,\mathrm{d}\theta, \quad EPE = \frac{1}{2}D_1D_2 \iint (\psi_1 - \psi_2)^2 \, r \,\mathrm{d}r \,\mathrm{d}\phi, \tag{2.7b}$$

$$RS_j = D_j \iint \left(r\frac{\partial}{\partial r}\frac{U_{j\phi}}{r}\right)\left(\frac{1}{r}\frac{\partial \psi_j}{\partial \phi}\right)\left(\frac{\partial \psi_j}{\partial r}\right) r \,\mathrm{d}r \,\mathrm{d}\phi \tag{2.7c}$$

$$PEC = D_1D_2 \iint (U_{1\phi} - U_{2\phi})\,\psi_1 \frac{1}{r}\frac{\partial \psi_2}{\partial \phi} \, r \,\mathrm{d}r \,\mathrm{d}\phi. \tag{2.7d}$$

The energy of perturbations to the mean flow (E) is a sum of the so-called eddy kinetic energy ($\sum EKE_j$) and eddy potential energy (EPE). Thus energy tendency $\partial_t E$

is balanced by the volume-integrated Reynolds Stresses work ($\sum RS_j$) and by Potential Energy Conversion (PEC), i.e., conversion rates from mean kinetic and mean potential energy, respectively (Pedlosky 1987). When the net perturbation energy tendency (i.e., left hand side of (2.7*a*)) is positive (i.e, perturbations grow), we may define a purely baroclinic instability as one where the Reynolds stresses volume-integrated work is zero, as occurs in uniform rectilinear flow (Pedlosky 1987). We later show that when RS_j do not vanish, they in fact are negative, i.e., decrease the perturbation growth rate in all cases we study here.

Bathymetry does not enter the energy equation explicitly: it does contribute to energy exchange locally, but integrates to zero over the entire domain. The energy equation has zero energy tendency for an azimuthally constant perturbation, and therefore such perturbations are necessarily neutral. RS_j are identically zero when the radial strain,

$$S_r \equiv r\frac{\partial}{\partial r}\frac{U_{j\phi}}{r}, \tag{2.8}$$

is identically zero, which in an annular channel occurs everywhere only for flow in solid-body rotation. Therefore solid body rotation is the only annular flow that has zero Reynolds stresses volume-integrated work for any infinitesimal perturbation. If S_r is nonzero anywhere then there exist many particular $\psi(r,\phi)$ perturbation shapes that make RS_j nonzero.

2.4. *Mean flow profiles*

Throughout this paper we compare our results against the case of uniform flow in a straight channel over linear bathymetry (Pedlosky 1964; Mechoso 1980), which is described in Appendix B. We hereafter refer to this case as uniform rectilinear flow for short. In the annular channel, we investigate in detail two specific configurations of the bathymetry and the mean azimuthal flow. Since the mean flows we prescribe are geostrophic, the isopycnal profile $Z_I(r)$ is determined by the Margules relation (Cushman-Roisin 1994). In dimensional variables,

$$\tilde{U}_{1\phi} - \tilde{U}_{2\phi} = -\frac{g'}{f}\frac{\partial \tilde{Z}_I}{\partial \tilde{r}}. \tag{2.9}$$

The first case, solid body rotation, is motivated by the fact that both uniform rectilinear flow and solid-body rotation have zero strain rate, defined for solid body rotation by (2.8), and thus it is a simple starting point from which to study the effect of horizontal curvature. We assume parabolic bathymetry to simplify the analysis, though we later briefly explore linear bathymetry too (see §6). Formally, we define our solid body rotation case as

$$U_{j\phi} = \Omega_j r, \quad Z_I \sim -(\Omega_1 - \Omega_2)r^2, \quad \eta_b = \frac{1}{2}pr^2, \tag{2.10}$$

where Ω_j are the constant angular velocities of the flow in each layer, and p is a quadratic coefficient for the bathymetry.

The second case is uniform azimuthal flow, where we assume constant mean azimuthal velocity everywhere. This is similar to uniform rectilinear flow in that the speed is uniform, and the isopycnals are linear in the cross-flow coordinate (r). It is different in that the velocity direction varies, i.e., speed is everywhere azimuthal but the azimuthal direction varies with the azimuthal angle ϕ. We take the bathymetry to be linear as well (as in the uniform rectilinear flow case), though we later briefly explore parabolic bathymetry as well (see §6). Formally, we define our uniform azimuthal flow case as

$$U_{j\phi} = \text{constants}, \quad Z_I \sim -(U_{1\phi} - U_{2\phi})r, \quad \eta_b = br, \tag{2.11}$$

where $U_{1\phi}$ and $U_{2\phi}$ are the azimuthal velocities and b is the linear coefficient for the bathymetry.

We note that in uniform azimuthal velocity R_i cannot be chosen to approach $r = 0$, both because the azimuthal velocity must be zero in the $r \to 0$ limit, and because even before the actual limit, the centrifugal force becomes larger than the Coriolis force, in violation of the QG conditions. The balance between the two forces results in a local Rossby number, $\mathrm{Ro} = U/f\tilde{r} = U/(r\sqrt{g'H_1H_2/(H_1+H_2)})$. For example, taking $H_1 = H_2 \approx 500m$, $g' \approx 10^{-3}g$, and $U \approx 0.1m/s$, we have $r > 1$ (and $R_i > 1$) as an approximate condition for $\mathrm{Ro} = o(1)$. Therefore our choice of $R_i = 3$ (§2.2) is also consistent with the QG approximation.

We define the mean vertical rotation rate shear and velocity shear for solid body rotation and for uniform azimuthal flow as follows: $\Omega_s = \Omega_1 - \Omega_2$, and $U_s = U_{1\phi} - U_{2\phi}$, respectively. Motivated by the fact that the baroclinic instability growth rate in uniform rectilinear flow varies linearly in the vertical velocity shear (Mechoso 1980), we choose the velocity scale $U = L\tilde{\Omega}_s$ for solid body rotation, and $U = \tilde{U}_s$ for uniform azimuthal flow. We assume everywhere that $U > 0$ (and hence $Z_I(r)$ is monotonously decreasing). This assumption is general since we explore both positive and negative δ and can then deduce corresponding results for $U < 0$ results by symmetry (see §5.3).

Similarly we define for solid body rotation and uniform azimuthal flow, the barotropic mean rotation rate and velocity as follows: $\Omega_{bt} = \frac{1}{2}(\Omega_1 + \Omega_2)$, and $U_{bt} = \frac{1}{2}(U_{1\phi} + U_{2\phi})$, respectively. In fact Ω_{bt} (or U_{bt}) is exactly the barotropic component only if mean layer thicknesses are equal, but for ease of notation we refer to it as the barotropic component in what follows.

3. Integral constraints on baroclinic growth

The classical theorem by Rayleigh (1880) on flow instability conditions was adapted by Pedlosky (1964) to the straight-channel rotating-baroclinic instability problem. It gives necessary (though not always sufficient) conditions for instability to occur, using only knowledge of the mean flow. Equivalently, the theorem provides a range of values for the physical parameters over which linear perturbations cannot grow. Here we adapt Pedlosky's derivation to the annular channel case, and use it to derive stability bounds for the profiles described in §2.4. The derivation and the results remain unchanged if $R_i \to 0$ and also if $R_e \to \infty$, and so are also applicable to other phenomena, e.g., geophysical vortices (Olson 1991; Paldor & Nof 1990; Dewar & Killworth 1995; Benilov 2005).

While qualitatively similar instability theorems have been derived in the literature for a variety of flows (Pedlosky 1970), we were unable to find this derivation or result elsewhere for azimuthal flow (QG or not) over bathymetry with no further constraints (e.g. thin layers, flat bottom). We also derived bounds on the phase speed and on the growth rate (semi-circle theorem, Pedlosky 1964) for general annular 2-layer flow, but we defer their presentation to Appendix C.

3.1. *Derivation of the Rayleigh theorem*

Our starting point is the modal PV equations (2.6*a*)-(2.6*b*). We define the complex phase speed $c = \sigma/m$, and its real (c_r) and imaginary (c_i) parts. By (2.5), only unstable eigenmodes have a non-zero c_i, so for unstable eigenmodes we may divide the equation

for the layer j by $m(U_{j\phi}/r - c)$.

$$\nabla_r^2\Psi_1 - \frac{m^2}{r^2}\Psi_1 - F_1(\Psi_1 - \Psi_2) - \frac{1}{U_{1\phi} - cr}\Psi_1\frac{\partial Q_1}{\partial r} = 0, \tag{3.1a}$$

$$\nabla_r^2\Psi_2 - \frac{m^2}{r^2}\Psi_2 - F_2(\Psi_2 - \Psi_1) - \frac{1}{U_{2\phi} - cr}\Psi_2\frac{\partial Q_2}{\partial r} = 0. \tag{3.1b}$$

We multiply the first and second of these last two equations by $D_1\Psi_1^*$ and $D_2\Psi_2^*$, respectively (where * denotes complex conjugate), and integrate with the volume element (rdr) between the domain boundaries R_i and R_e. The first (Laplacian) term can be simplified via integration by parts, making use of the boundary conditions $\Psi_j(R_i) = \Psi_j(R_e) = 0$. The result is

$$\int_{R_i}^{R_e}\left[\sum_{j=1}^{2} D_j\left|\frac{\partial}{\partial r}\Psi_j\right|^2 + \sum_{j=1}^{2} D_j\frac{m^2}{r^2}\left|\Psi_j\right|^2 + D_1D_2\left|\Psi_1 - \Psi_2\right|^2\right] r\,\mathrm{d}r + \int_{R_i}^{R_e}\left[\sum_{j=1}^{2}\frac{D_j}{U_{j\phi} - cr}\frac{\partial Q_j}{\partial r}\left|\Psi_j\right|^2\right] r\,\mathrm{d}r = 0. \tag{3.2}$$

The imaginary part of this expression is

$$c_i\int_{R_i}^{R_e}\sum_{j=1}^{2}\frac{D_j}{\left|U_{j\phi} - cr\right|^2}\frac{\partial Q_j}{\partial r}\left|\Psi_j\right|^2 r^2\mathrm{d}r = 0. \tag{3.3}$$

For an unstable mode c_i is nonzero, and so the last integral must vanish. Therefore a necessary condition for instability (hereafter, the Rayleigh criterion) is that the mean PV gradient must be somewhere negative and somewhere positive in the domain interior.

Another necessary condition for instability can be found using the real part of (3.2). Substituting (3.3) into (3.2), eliminates ther terms proportional to c_r and c_i, leaving

$$\int_{R_i}^{R_e}\sum_{j=1}^{2}\frac{D_j}{\left|U_{j\phi} - cr\right|^2}\left|\Psi_j\right|^2\left(U_{j\phi}\frac{\partial Q_j}{\partial r}\right) r\,\mathrm{d}r = -\int_{R_i}^{R_e}\left[\sum_{j=1}^{2} D_j\left|\frac{\partial}{\partial r}\Psi_j\right|^2 + \sum_{j=1}^{2} D_j\frac{m^2}{r^2}\left|\Psi_j\right|^2 + D_1D_2\left|\Psi_1 - \Psi_2\right|^2\right] r\,\mathrm{d}r < 0. \tag{3.4}$$

Therefore, another necessary instability condition (hereafter, the Fjortoft criterion) can be stated as: at least one of the products $U_{1\phi}\frac{\partial Q_1}{\partial r}$ and $U_{2\phi}\frac{\partial Q_2}{\partial r}$, must be negative inside at least part of the domain (R_i, R_e).

Both the first and second conditions as phrased here are the same as found in a straight-channel (Pedlosky 1964). These (straight channel) conditions are used frequently to identify unstable flow regimes in boundary currents, as well as other ocean and atmosphere flow regimes.

3.2. *Stability bounds for solid-body rotation and uniform azimuthal flow*

For solid body rotation, using the same notation as (Mechoso 1980) the ratio between bathymetric slope and isopycnal slope is the bathymetric parameter $\delta = pr/\Omega_s r = p/\Omega_s$. Vorticity is constant and hence the PV gradients are simply

$$\frac{\partial Q_1}{\partial r} = -F_1 r, \quad \frac{\partial Q_2}{\partial r} = F_2\left(1 - \delta\right) r. \tag{3.5}$$

By the Rayleigh criterion instability is possible only if the PV gradient changes sign, which is seen from (3.5) to occur only if $\delta < 1$, exactly as in uniform rectilinear flow.

For uniform azimuthal flow, in non-dimensional variables, $U_{1\phi} = U_{2\phi} + 1$. The bathymetric parameter is now $\delta = -b$, and from equation (2.6c),

$$\frac{\partial Q_1}{\partial r} = -\frac{1}{r^2}\left(U_{2\phi}+1\right) - F_1, \quad \frac{\partial Q_2}{\partial r} = -\frac{1}{r^2}U_{2\phi} + F_2\left(1-\delta\right). \tag{3.6}$$

Using (3.6) in the instability criteria (§3.1), it follows that a necessary condition for instability is that, at least somewhere inside the domain,

$$\delta < \delta_0(r) \equiv 1 - \frac{1}{F_2}\frac{U_{2\phi}}{r^2}. \tag{3.7}$$

Equivalently, a sufficient condition for stability is $\delta > \max(\delta_0)$, similarly to the uniform rectilinear flow case which is stable for $\delta > 1$. Note that $\delta_0 = 1$ exactly if $U_{2\phi} = 0$, and $\delta_0 \approx 1$ if $\frac{1}{F_2}\frac{|U_{2\phi}(r)|}{r^2} = o(1)$. Unlike the case in uniform rectilinear flow, the stability threshold depends on the mean velocity magnitude, i.e., the cutoff bathymetric parameter, δ_0, increases (decreases) for negative (positive) $U_{2\phi}$. As evident from the Rayleigh criterion and from (3.6), the difference is due to the non-zero mean relative vorticity caused by curved streamlines.

We add that for $U_{2\phi} < -1 - F_1 R_i^2$, instability is not prohibited, irrespectively of the δ value, since a PV gradient sign change occurs within a single layer. However, since the mean flow becomes almost barotropic, that regime is less relevant to this study.

4. Stability of flows in solid-body rotation

In this section, we investigate baroclinic instability of flow in solid body rotation, and show that it bears strong dynamical similarity to baroclinic instability of uniform rectilinear flow. The isopycnal cross-flow profile for solid-body rotation is parabolic (§2.4), and we specifically choose to investigate the flow over a cross-flow profile similar to the isopycnal profile, namely a parabolic bathymetry profile. This simplifies the PV equations significantly, and allows for some analytical results which help with more general interpretation of the physical system. Linear bathymetry does not qualitatively change the results, as discussed in §6.

In the solid body rotation case, equations (2.6a)-(2.6b) are,

$$\left[\left(\Omega_{bt}+\frac{1}{2}\right)m - \sigma\right]\left[\nabla_r^2\Psi_1 - \frac{m^2}{r^2}\Psi_1 - F_1(\Psi_1-\Psi_2)\right] + mF_1\Psi_1 = 0, \tag{4.1a}$$

$$\left[\left(\Omega_{bt}-\frac{1}{2}\right)m - \sigma\right]\left[\nabla_r^2\Psi_2 - \frac{m^2}{r^2}\Psi_2 - F_2(\Psi_2-\Psi_1)\right] + mF_2\Psi_2\left[-1+\delta\right] = 0. \tag{4.1b}$$

Since Ω_s does not appear explicitly, it follows from the scaling in section 2.4 that the dimensional growth rate and frequency depend linearly on the dimensional angular shear $\tilde{\Omega}_s$. In addition, the variables Ω_{bt} and σ appear only together, in the expression $(\Omega_{bt}m - \sigma) \equiv \sigma_0$. Solving (4.1) for σ_0 would correspond to a σ solution Doppler-shifted by $\Omega_{bt}m$. The only effect of the barotropic velocity is a real frequency Doppler-shift, with no influence on growth rate or streamfunction structure. Therefore to derive the dispersion relation we may take $\Omega_{bt} = 0$, and after deriving it, just Doppler-shift the frequency back by adding to it the term $\Omega_{bt}m$.

The terms in the left brackets may vanish only for neutral modes. In this section we are only interested in modal instability (non-normal growth is covered in §5.2) and hence

assume that the terms in the left brackets do not vanish and rearrange (4.1) to obtain a pair of coupled Bessel equations,

$$\nabla_r^2\Psi_1 - \frac{m^2}{r^2}\Psi_1 + \alpha_1\Psi_1 + F_1\Psi_2 = 0, \tag{4.2a}$$

$$\nabla_r^2\Psi_2 - \frac{m^2}{r^2}\Psi_2 + \alpha_2\Psi_2 + F_2\Psi_1 = 0, \tag{4.2b}$$

$$\alpha_1 = F_1\frac{\frac{1}{2}m+\sigma}{\frac{1}{2}m-\sigma}, \qquad \alpha_2 = F_2\frac{\left(\frac{1}{2}-\delta\right)m-\sigma}{\frac{1}{2}m+\sigma}. \tag{4.2c}$$

The solution can be found in terms of Bessel functions of the first kind J_m and of the second kind Y_m. A complete and orthogonal set of Bessel functions in the radial domain (R_i, R_e) can be found as the solution set of the Bessel equation in the same geometry with Dirichlet boundary conditions. This set is given by $P_m(\mu_i r)$,

$$P_m(\mu r) = J_m(\mu r) - \frac{J_m(\mu R_e)}{Y_m(\mu R_e)}Y_m(\mu r), \tag{4.3}$$

provided that μ_i are determined from

$$J_m(\mu_i R_i)Y_m(\mu_i R_e) - Y_m(\mu_i R_i)J_m(\mu_i R_e) = 0. \tag{4.4}$$

The general solution to (4.2) may be then expanded in the Fourier-Bessel series,

$$\Psi_j = \Sigma_{i=1}^{\infty} A_{j,i}P_m(\mu_i r). \tag{4.5}$$

The amplitudes $A_{j,i}$ are constants. Plugging the general solution (4.5) into (4.2), using the identity that a Bessel function of order m satisfies, $\nabla_r^2 P_m(\mu r) - \frac{m^2}{r^2}P_m(\mu r) = -\mu^2 P_m(\mu r)$, and exploiting the orthogonality of the P_m functions, one finds that the solution (4.5) is consistent, under the following condition on the coefficients of each Bessel function,

$$(\alpha_1 - \mu_i^2)A_{1,i} + F_1 A_{2,i} = 0, \tag{4.6a}$$

$$(\alpha_2 - \mu_i^2)A_{2,i} + F_2 A_{1,i} = 0. \tag{4.6b}$$

Requiring the determinant to disappear we find, after some algebra, the solid body rotation dispersion relation, relating the complex frequency σ to the radial wavenumber-like parameter μ_i,

$$\sigma_i = \Omega_{bt} + m\frac{\mu_i^2\left(F_2 - F_1 - F_2\delta\right) - mF_1F_2\delta + \sqrt{D}}{2\mu_i^4 + 2\mu_i^2\left(F_1+F_2\right)}, \tag{4.7a}$$

$$\begin{aligned}\frac{D}{m^2} =& \mu_i^8 + \left(2F_2\delta\right)\mu_i^6 + \left(-4F_1F_2 + 2F_1F_2\delta + F_2^2\delta^2\right)\mu_i^4 \\ &+ \left(-4F_2^2F_1\delta + 2F_2^2F_1\delta^2\right)\mu_i^2 + F_1^2F_2^2\delta^2.\end{aligned} \tag{4.7b}$$

The main result of this section is that the solid body rotation dispersion relation (4.7) is isomorphic to the uniform rectilinear flow dispersion relation (B 2), showing that the dynamics are in some sense identical, although the geometries are different. The mapping between the dispersion relations is symbolic (and simple), with $(\Omega_{bt}, m, \mu) \to (V_{bt}, l, K)$. Here k, l, $K = \sqrt{k^2+l^2}$, and V_{bt}, are the uniform rectilinear flow cross-stream, downstream, total wavenumbers, and mean barotropic velocity, respectively (see Appendix B). Since the dispersion relations are analogous, the dependences of the growth rates and frequencies on the dimensionless parameters are similar, though not identical since the allowed μ_i are determined from (4.4), while the allowed K are determined from an equation with harmonic functions instead of Bessel functions.

In figure 2 we display numerical dispersion curves (growth rates and phase speeds as a function of wavenumber m) for solid body rotation and for uniform rectilinear flow, setting $\delta = -0.2$ for the purpose of illustration. We normalize the azimuthal wavenumber by the mean radial coordinate $R = (R_1 + R_2)/2$, $\hat{m} = m/R$ to provide an approximate analogue of the Cartesian wavenumber in uniform rectilinear flow. The uniform rectilinear flow and solid body rotation curves are very close to each other, and the main qualitative features are identical for both cases: (i) two eigenmodes exist in each case (for other δ values either 1 or 2 eigenmodes but no more exist per downstream wavenumber). (ii) The global maximum in growth rate occurs at a wavenumber slightly smaller than 1 (in dimensional variables $l \approx 1/L$). (iii) The phase speed has the opposite sign to δ. This is in fact true for all δ values and is explained by a resonance condition (Pichevin 1998) with topographic Rossby waves (which propagate with shallow water to their right in the northern hemisphere). Panels (c) and (d) show a typical first (fastest growing) eigenmode streamfunction for solid body rotation. The streamfunction is centered in the channel, and no mean horizontal tilt (relative to the cross-stream direction) is present in the circulation cells. The second fastest growing eigenmodes (not shown) have two periods in the radial axis, rather than one as the first mode, and are generally similar to the first mode in that they have no horizontal tilt.

Figure 3b shows the solid body rotation growth rate as a function of both m and δ. Again, the growth rate values are almost identical to the uniform rectilinear flow case (figure 3a). We also confirmed numerically that (as in uniform rectilinear flow) there is no growth rate dependence on barotropic velocity. Thus we can summarize the solid body rotation case as follows: (i) The dispersion relation is isomorphic to the previously-derived uniform rectilinear flow dispersion relation, thus demonstrating that the dynamics are essentially identical. The growth rate is independent of the barotropic velocity and linearly dependent on the vertical shear. Thus, (ii) despite different geometries (affecting the boundary conditions) in solid body rotation and in uniform rectilinear flow, the growth rates are very similar (figure 3a and b). (iii) Both cases have vanishing strain rates and RS_j and are thus pure baroclinic instabilities.

5. Stability of uniform azimuthal flow

In this section we explore the stability of uniform azimuthal flow over bathymetry that varies linearly with radius, as defined in §2.4.

5.1. *Normal modes*

In figure 3, we plot growth rate (GR) as a function of normalized wavenumber $\hat{m}$ and of δ for uniform azimuthal flow (each panel for a different U_{bt} value), and for reference also the GR of the uniform rectilinear flow and solid body rotation cases. Note that at each point in $(\hat{m}, \delta)$ space there may be multiple unstable modes, so we have plotted the growth rate of the most unstable mode in each case. While for zero barotropic flow $U_{bt} = 0$ the growth rate is similar to uniform rectilinear flow, nonzero barotropic velocity results in very different $\mathrm{GR}(\hat{m}, \delta)$ dependence. In contrast, uniform rectilinear flow and solid body rotation have no barotropic velocity dependence. Additional local maxima in $\mathrm{GR}(\hat{m}, \delta)$ appear in uniform azimuthal flow for nonzero barotropic velocity.

The streamfunctions for several unstable uniform azimuthal flow modes are presented in figure 4. Two geometrical differences from uniform rectilinear flow and solid body rotation (see examples in figure 2) are evident: (a) While in solid body rotation streamfunctions are always centered in the channel, the streamfunctions in uniform azimuthal flow cases with nonzero U_{bt} are shifted off the center of the channel. (b) While in

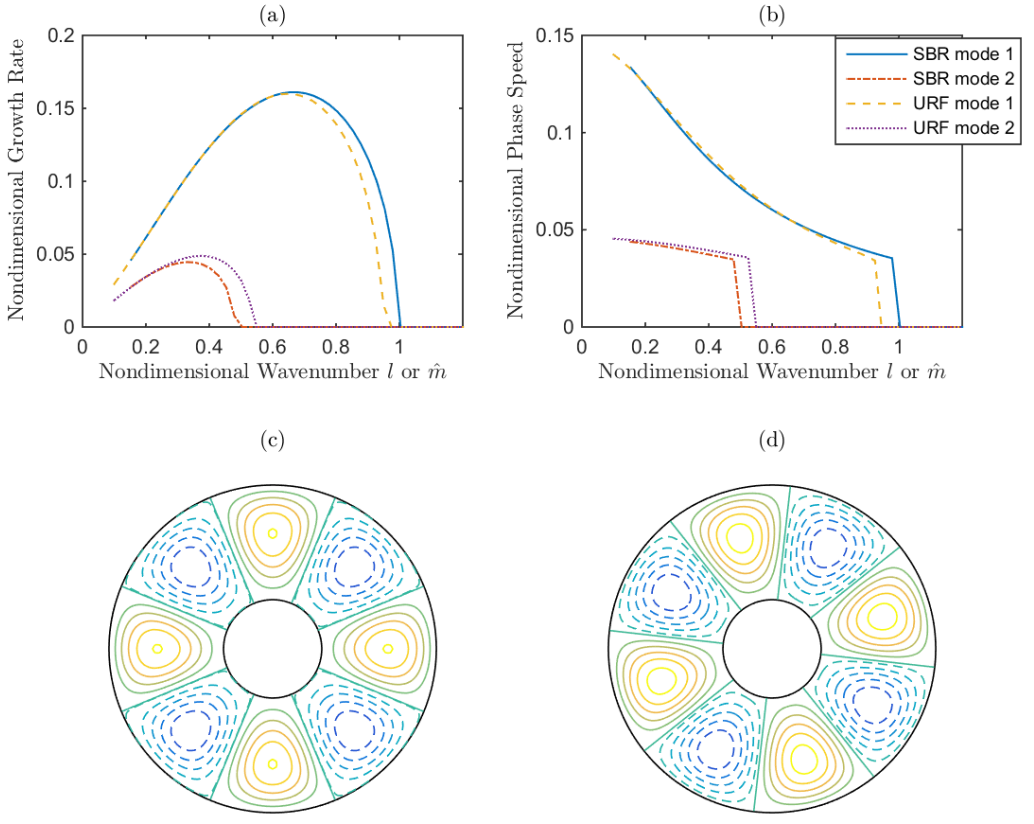

FIGURE 2. Properties of unstable modes for mean solid body rotation over parabolic bathymetry and for mean uniform rectilinear flow over linear bathymetry, with $\delta = -0.2$ in both cases. (a) Growth rate vs wavenumber and (b) phase velocity vs wavenumber (all dimensionless). In both cases two independent eigenmodes are found. The first (second) mode is presented with solid and dashed/dotted lines for solid body rotation (SBR) and uniform rectilinear flow (URF), respectively. The abscissa is downstream Cartesian wavenumber (nondimensional values). In solid body rotation the downstream wavenumber is defined as $l \approx \hat{m} = m/R$. Here m is the azimuthal wavenumber and R is the radius of the channel center. In panel (b) the (real) phase speed is approximately Doppler-corrected and normalized to Cartesian values (for comparison with uniform rectilinear flow) via $\hat{c}_r = c_r R - \Omega_{bt}$. (c,d) Upper and lower layer streamfunctions, respectively, for the first (fastest growing) eigenmode of solid body rotation with wavenumber $m = 4$ ($\hat{m} = 0.615$). The inner and outer circles mark the domain boundaries at $r = R_i$ and R_e, respectively. The lines intercepting the boundaries are the zero contours of the streamfunctions, while positive (negative) streamfunction contours are denoted by full (dashed) closed curves. The absolute value of contours is not given since eigenmode amplitudes are arbitrary unless specified by initial conditions.

uniform rectilinear flow the streamfunction circulation cells axes are aligned with the radial direction, those in uniform azimuthal flow cases with nonzero U_{bt} are often tilted. Reynolds stress work varies linearly with the strain and the tilts of the circulation axes, and vanishes when the tilt is zero (Pedlosky 1987). In polar coordinates,

$$RS_j \sim -(S_r)_j \left(\frac{\partial r}{\partial \phi} \right)_{\psi_j} . \tag{5.1}$$

The uniform azimuthal flow streamfunction for the first mode at $U_{bt} = 0$ (left panel)

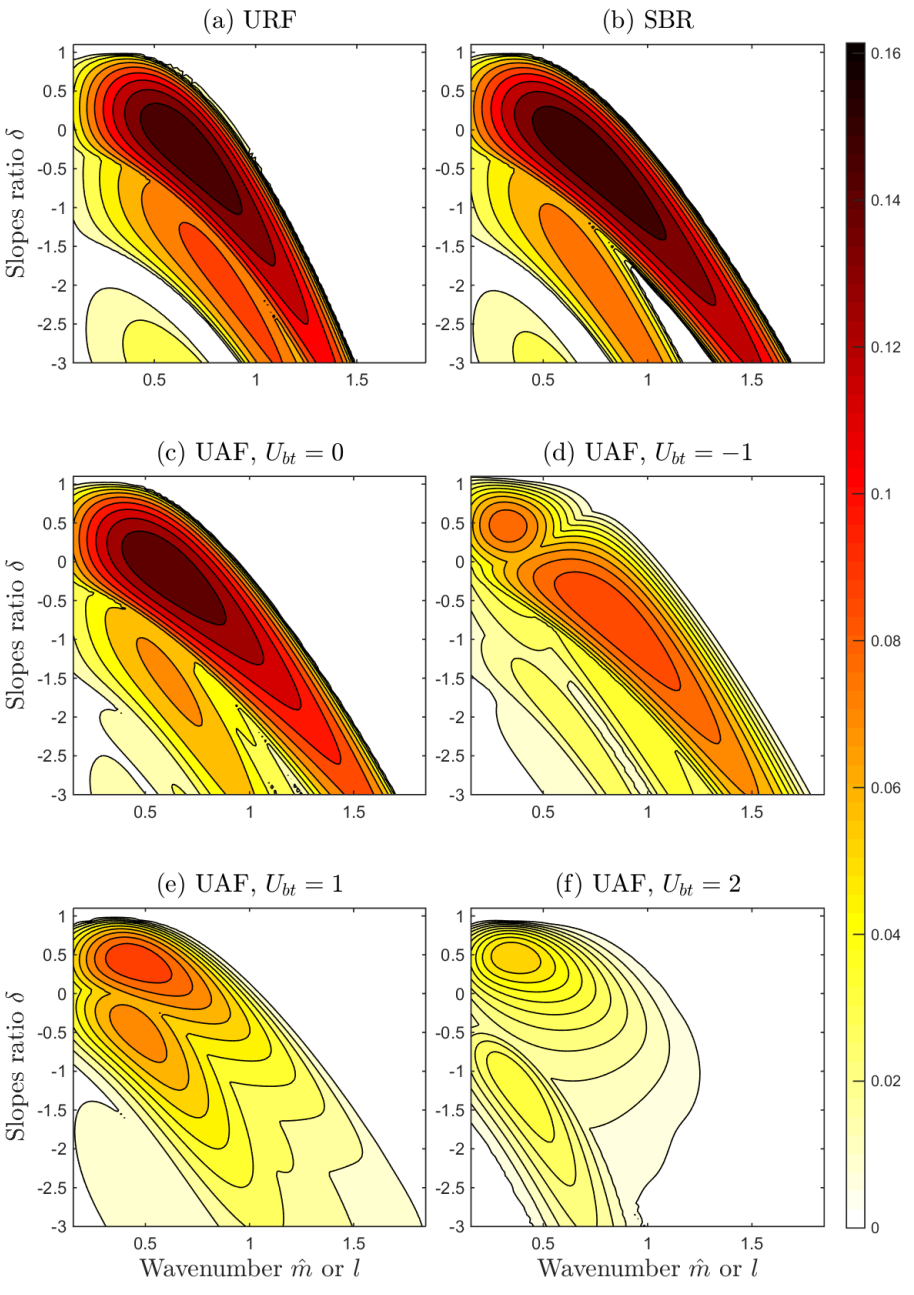

FIGURE 3. Linear growth rates as a function of along-flow wavenumber and the ratio of the bathymetric to isopycnal slopes. All values are non-dimensionalized as described in §2.1. Where more than one unstable modes exist, the highest growth rate is shown. (a) Mean uniform rectilinear flow (URF) over linear bathymetry, with wavenumber l. In all other panels the wavenumber is the normalized azimuthal wavenumber $\hat{m}$, defined in §4. (b) Mean solid body rotation (SBR) over parabolic bathymetry. (c–f) Mean uniform azimuthal flow (UAF) over linear bathymetry, with with the mean barotropic velocity equal to (c) $U_{bt} = 0$, (d) $U_{bt} = -1$, (e) $U_{bt} = 1$, and (f) $U_{bt} = 2$. In contrast to uniform azimuthal flow, the growth rates in the uniform rectilinear flow and solid body rotation cases do not depend on the barotropic velocity.

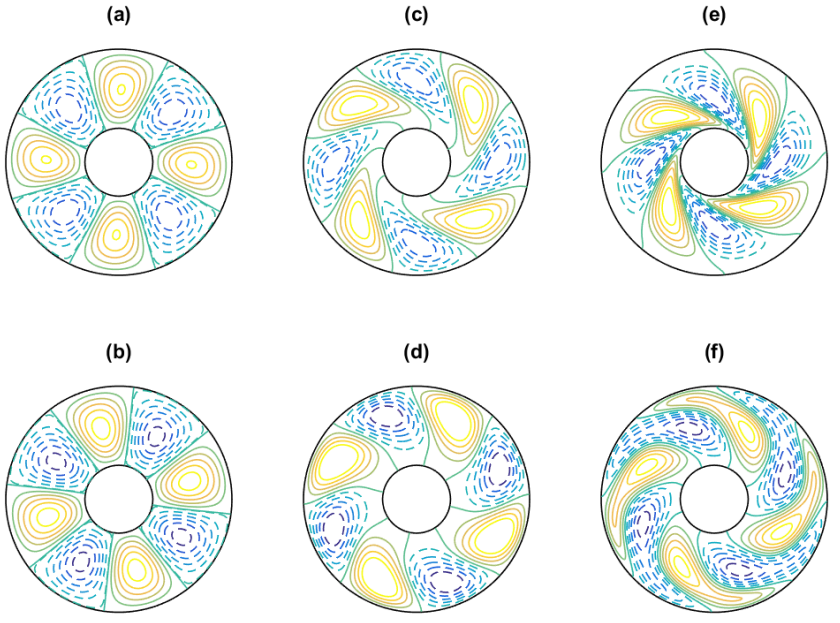

FIGURE 4. Mean uniform azimuthal flow, selected unstable eigenmodes. Upper (lower) layer streamfunctions are shown in the upper (lower) panels. The bathymetric slope parameter is $\delta = -0.2$, and the azimuthal wavenumber is $m = 4$. (a,b) $U_{bt} = 0$, fastest growing eigenmode. (c,d) $U_{bt} = -1$, fastest growing eigenmode. (e,f) $U_{bt} = -1$, third-fastest growing eigenmode. The inner and outer circles mark the domain boundaries at $r = R_i$ and R_e, respectively. The lines intercepting the boundaries are the zero contours of the streamfunctions, while positive (negative) streamfunction contours are denoted by full (dashed) closed curves. The absolute value of contours is not given since eigenmode amplitudes are arbitrary unless specified by initial conditions.

has zero or very small tilt, implying insignificant Reynolds stresses work. The center and right panels (for the first and third eigenmodes with $U_{bt} = -1$) show progressively higher positive tilts, implying higher negative RS_j, since by (2.8) strain rate is positive for constant negative velocity.

The local maxima in the panels (d)-(f) of figure 3 are due to changes in the number and character of growing eigenmodes with U_{bt} value. This can be seen in figure 5, where we plot several properties for all uniform azimuthal flow growing eigenmodes at $\delta = -0.2$ and $U_{bt} = 1$ (compare with solid body rotation and uniform rectilinear flow, figure 2). We find that up to four unstable eigenmodes can co-exist at a given wavenumber, whereas no more than two co-existed for uniform rectilinear flow and solid body rotation. While in uniform rectilinear flow the second mode has considerably lower growth rate than the first, in uniform azimuthal flow they have similar maximum values but still peak at different wavenumbers, thus explaining the multiple maxima observed in figure 3 panels (d)-(f). The growth rates of third- and fourth-most unstable modes are considerably smaller. In figure 5(c) we plot the eigenmodes' phase speeds, doppler-corrected and normalized via $\hat{c}_r = c_r R - U_{bt}$ to compare approximately with equivalent values in uniform rectilinear flow. While uniform rectilinear flow has waves propagating with shallow water to their right (prograde), in uniform azimuthal flow the second most rapidly growing mode is retrograde, and eigenmodes 3 and 4 have much smaller propagation speeds $\hat{c}_r$.

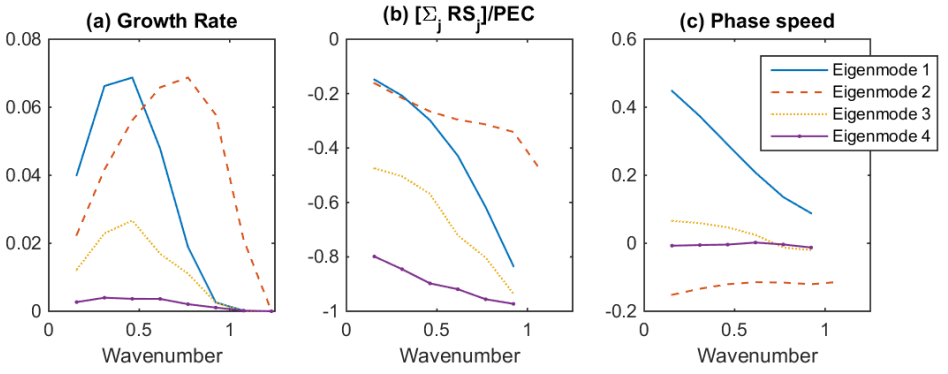

FIGURE 5. Mean uniform azimuthal flow with barotropic velocity $U_{bt} = 1$ and bathymetric to isopycnal slopes ratio $\delta = -0.2$. (a) Growth rate, (b) ratio of Reynolds stresses volume-integrated work to potential energy conversion, and (c) Doppler-corrected Cartesian phase speed vs normalized azimuthal wavenumber $\hat{m} = m/R$, for all growing eigenmodes. In panel (c) the (real) phase speed is Doppler-corrected and normalized to Cartesian values by $\hat{c}_r = c_r R - U_{bt}$, to facilitate comparison with the other mean flow cases (figure 2).

The middle panel of figure 5 shows the ratios of volume-integrated Reynolds stress work ($\Sigma_j RS_j$) to potential energy conversion (PEC), which are negative in all cases. In contrast, uniform rectilinear flow has zero RS_j values in all cases. Thus the uniform azimuthal flow unstable eigenmodes are largely baroclinic modes whose growth rates are somewhat diminished by Reynolds stresses work. The two extra eigenmodes that appear with non-zero barotropic velocity have much higher $\Sigma_j RS_j$ to PEC ratio magnitudes, consistent with their very low growth rates. These results are also consistent with the tilts of streamfunctions shown in figure 4, and are qualitatively similar for other values of δ, m and U_{bt}. The general reduction in growth rate with $|U_{bt}|$ is thus partially attributed to increase in Reynolds stresses work.

In figure 6 (panels a and b) we plot the maximum growth rate over all unstable modes and over all wavenumbers as a function of U_{bt} and δ. Unless $\delta \sim 1$, the growth rate peaks at or close to $U_{bt} = 0$, and is close to peak growth rate for the uniform rectilinear flow case, while lower growth rates are found for non-zero U_{bt}. However, the uniform rectilinear flow instability has a cutoff at $\delta = 1$, whereas the uniform azimuthal flow cutoff depends on U_{bt} and can occur for δ larger than 1, as predicted by the instability criteria derived in §3.2. Therefore horizontal curvature decreases eigenmodes' growth rates when U_{bt} is non-zero, unless the isopycnals are approximately parallel to the bathymetry ($\delta \sim 1$) and $U_{bt} < 0$, in which case the curvature destabilizes the flow. Although we report above that Reynolds stresses work is partially responsible for reduction in growth rate (both relative to uniform rectilinear flow and between different uniform azimuthal flow modes), figure 6c demonstrates that reduction in potential energy conversion is responsible for a $\sim 2-4$ times larger fraction of the growth rate reduction, than is the $|\Sigma_j RS_j|$ increase. For an eigenmode, $GR = (PEC + \Sigma_j RS_j)/2$ and hence the changes in growth rate are proportional to changes in PEC and RS_j. Generally PEC decreases monotonously with $|U_{bt}|$, thus supporting the barotropic governor effect interpretation, given below.

Reduction in baroclinic growth rate in the presence of lateral barotropic shear is a somewhat general phenomenon, often called barotropic governor effect (James & Gray 1986; James 1987). James (1987) attributes the effect to the horizontal shear of advection. To remain in phase in the cross-flow direction in the presence of advective shear, the unstable eigenmodes are tilted in the horizontal plane and have a reduced cross-flow

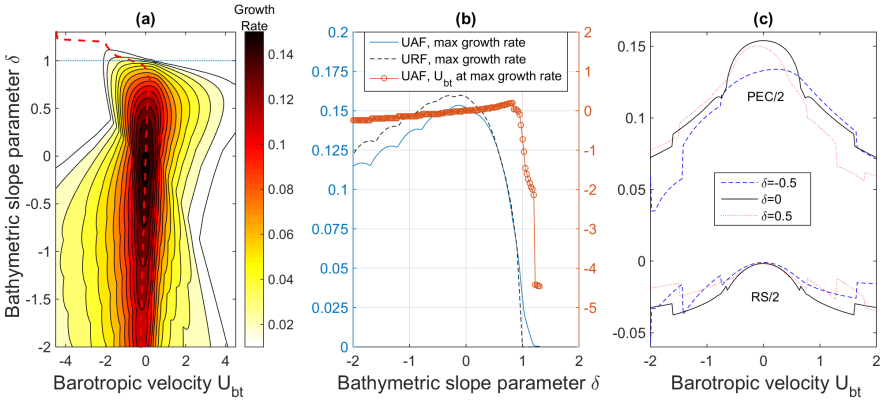

FIGURE 6. (a) Maximum growth rate (filled contours) in the uniform azimuthal flow (UAF) case as a function of the barotropic velocity, U_{bt}, and the ratio of the bathymetric to isopycnal slopes, δ. The dashed line marks the barotropic velocity corresponding to the largest growth rates at each δ. The dotted line marks $\delta = 1$, above which straight channel uniform flow is stable. (b) Maximum uniform azimuthal flow growth rate (full line) and the barotropic velocity at which it is achieved (full line with circles), as a function of δ. The dashed line is maximum growth rate for uniform rectilinear flow (URF). (c) (Half the value of) Potential Energy Conversion (PEC) and Reynolds stresses work ($RS = \Sigma_j RS_j$), for the fastest growing eigenmode, in three different δ values. Discontinuities (as a function of U_{bt}) are expected since $PEC - RS$ distribution changes with m, and since up to four different eigenmodes exist per m.

extent. These circulation features make the unstable eigenmodes less ideally suited for extracting mean potential energy and hence their growth rates are smaller.

Though the usual barotropic governor effect interpretation is due to barotropic shear, we find that in curved flow geometry, it may be more general to refer to barotropic strain rather than shear. In uniform azimuthal flow, the eigenmodes are azimuthally traveling waves, with constant angular phase velocity [rad/s]. If they were to have no tilt, azimuthal advection would need to be radially constant. The azimuthally advecting quantity is the (mean) angular velocity, $\Omega_j(r) \equiv U_{j\phi}/r$, and its radial gradient is the strain rate (2.8). Thus the barotropic governor effect can generally occur in azimuthal flow with non-zero strain, i.e. flow not in solid-body rotation (§4). In accordance, we find (figure 4) that some uniform azimuthal flow eigenmodes have substantial horizontal tilts, often with much lower growth rates. Similar results were obtained in a primitive-equations 2-layer vortex instability model Dewar & Killworth (1995). The authors found that Gaussian vortices with co-rotating lower layers had reduced PEC and growth rates relative to vortices with counter-rotating lower layers, and attributed the result to the barotropic governor effect.

5.2. *Non-normal growth*

While the above diagnosis focuses on perturbation growth by individual eigenmodes (aka normal modes), non-orthogonality of eigenmodes, which is a common occurrence in sheared flow, means that what is known as non-normal growth is also possible (Trefethen *et al.* 1993; Farrell & Ioannou 1996). Linear evolution of two or more non-orthogonal eigenmodes, even if they are all neutral or decaying, can result in transient (non-normal) growth before the eventual decay of the disturbance. For parameter values where growing eigenmodes exist, they do dominate the linearized dynamics, at long enough times. But transient non-normal growth may dominate at shorter times, as well as for parameter ranges where no growing eigenmodes exist.

To calculate the non-normal growth, using the same numerical eigenvalue solver described above, we recast the PV equations (2.6) in the form: $M\Psi = \sigma B\Psi$, where M and B are differential operators, and $\Psi = (\Psi_1, \Psi_2)^T$ (T for transpose). We refer the reader to Farrell & Ioannou (1996) for details of the method. Assuming B is invertible we can rewrite the differential equation as $\sigma\Psi = L\Psi$, where $L = B^{-1}M$. And since $\Psi \sim \exp(-i\sigma t)$,

$$\partial_t \Psi = -iL\Psi. \tag{5.2}$$

So the propagator to time t is $\exp(-iLt)$. If we define $\hat{L} = N^{1/2}LN^{-1/2}$, where N is the energy norm operator (Farrell & Ioannou 1996), then the maximal instantaneous growth-rate of disturbances is given by the eigenvalues (and eigenstates) of the operator $H = \frac{1}{2}i(\hat{L}^\dagger - \hat{L})$. The energy-norm operator in the annulus case is, prior to the performed discreziation of the differential operators and of r,

$$N = \frac{1}{2}\begin{pmatrix} rD_1 & 0 \\ 0 & rD_2 \end{pmatrix}\left(-\nabla_r^2 + \frac{m^2}{r^2}\right) + \frac{1}{2}D_1 D_2 \begin{pmatrix} 1 & -1 \\ -1 & 1 \end{pmatrix}. \tag{5.3}$$

In figure 7 the maximal instantaneous non-normal growth in energy norm is shown for uniform azimuthal flow and uniform rectilinear flow. Interestingly, the result is independent of δ, as the bathymetry does not appear in the energy equation (2.7). Bathymetry affects local energy conversion but not its domain integral. However, in finite time bathymetry certainly effects energy growth or decay since it affects the streamfunction evolution, and would likely render sub-optimal the fastest-growing non-normal perturbations calculated using (5.3). For $U_{bt} = 0$, uniform azimuthal flow growth is very similar to uniform rectilinear flow (which is independent of barotropic velocity), and both have non-normal growth just slightly higher than peak normal growth rate (compare with figure 6). However, non-normal growth occurs for a wider range of wavenumbers than the range in which unstable normal modes exist. The decay of the non-normal growth rate with wavenumber is slower in uniform azimuthal flow relative to uniform rectilinear flow. In addition, at nonzero U_{bt}, the uniform azimuthal flow growth rate is higher everywhere, and decays even slower with $\hat{m}$, or even (not shown) grows and oscillates in $\hat{m}$ before decaying again. Growth at very high wavenumbers is probably not physical, and would likely not appear if some form of scale-selective "eddy" viscosity were included.

5.3. *Convex and concave cases*

The convex to concave transformation (by reflection of $\eta_b(r)$ and $Z_I(r)$, as explained in §2.1), results for uniform azimuthal flow in $b \to -b$ and $U_{j\phi} \to -U_{j\phi}$. Therefore equations (2.6) are unaltered if in addition $\sigma \to -\sigma$. Also, if $\{\sigma, \Psi_j(r)\}$ are an eigenvalue-eigenfunction pair of equations (2.6) then so are their complex conjugates $\{\sigma^*, \Psi_j^*(r)\}$, as can be verified by taking the complex conjugate of (2.6). Combining the last two observations, if $\{\sigma, \Psi_j(r)\}$ is an eigenvalue-eigenfunction pair in a convex geometry, then $\{-\sigma^*, \Psi_j^*(r)\}$ is an eigenvalue-eigenfunction pair in a concave geometry, and vice-versa. Thus the growth rate and the real (physical) part of the streamfunction are unaltered, and the phase speed is reversed. The reversal of phase speed, along with reflection of $\eta_b(r)$ (shallow water at other side of the channel) results in the same phase speed direction relative to shallow water, and therefore the physical propagation direction is also unaltered.

Different eddy growth rate at convex versus concave sections is not accounted for in the linear uniform azimuthal flow model, contrasting with the pronounced instabilities observed around convex bends in the real ocean's continental slopes (see §1). Despite

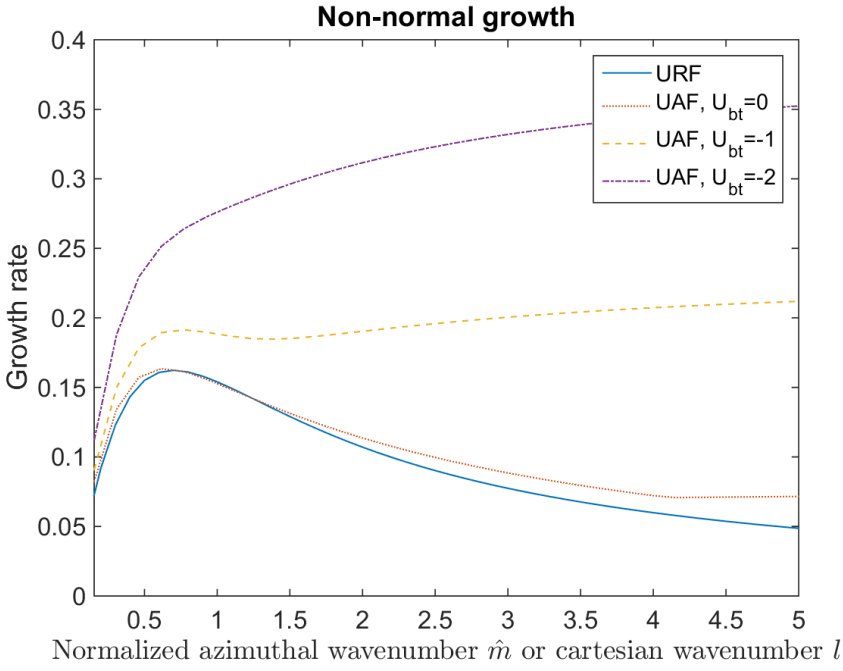

FIGURE 7. Maximal instantaneous (non-normal) growth rates. The blue curve corresponds to mean uniform rectilinear flow. The other curves correspond to mean uniform azimuthal flow with three different barotropic velocities U_{bt}. Linear bathymetry was used in all cases.

this symmetry of our QG model, there is still a potentially important difference between unstable modes growing over convex and concave bends in the continental slope. If the perturbation streamfunction is displaced off the center of the channel, say toward shallower water, then switching between concave and convex continental slopes will result in the streamfunction being displaced toward deep water instead. As noted in §5.1, the uniform azimuthal flow perturbation streamfunctions are indeed typically displaced from the center of the channel (see figure 4). The significance of this difference between structure of growing modes over convex and concave continental slopes cannot be determined from our linear instability analysis, and warrants further investigation using a nonlinear model.

6. Relation between baroclinic instability in straight and curved geometries

Although uniform azimuthal flow and uniform rectilinear flow share the same cross-stream isopycnal and bathymetric profiles, the properties of their unstable modes are quite different (§5). In contrast, we found strong similarity (§4) between the uniform rectilinear flow and solid body rotation cases, despite differing isopycnal and bathymetric profiles. Using insights from §4-5, we can reduce the parallel between uniform rectilinear flow and solid body rotation to three conditions:

(i) Vanishing horizontal mean strain, resulting in zero Reynolds stresses work. From a dynamical perspective, the mean flow does not shear waves propagating in the direction of the mean flow.

The following two factors stem from the Rayleigh criterion (§3).

(ii) Vanishing horizontal gradient of the mean vorticity. Under this condition the Rayleigh criterion depends only on the ratio of bathymetric to isopycnal slopes, δ.

(iii) Congruous cross-stream bathymetric and isopycnal profiles. This renders δ constant. The implication can be understood by considering a uniform rectilinear flow-like case of uniform channel flow (linear isopycnals) but over non-linear bathymetry. Then, using (2.9) and defining $\delta(x) = \frac{\partial \eta_b(x)}{\partial x} / \frac{\partial Z_I}{\partial x}$, the PV gradient (B 1) can be rewritten as

$$\frac{\partial Q_j}{\partial x} = -F_j(-1)^j \left[1 - \Delta_{j2}\delta(x)\right]. \tag{6.1}$$

By the Rayleigh criterion (§3) if $\delta(x) < 1$ anywhere, instability is not prohibited. Thus even if $\bar{\delta} > 1$ (the bar denoting a cross-stream average), but locally $\delta(x) < 1$ somewhere, then this uniform flow case may be unstable.

For annular flow, the vanishing of the strain rate occurs only for parabolic isopycnals (or equivalently, solid-body rotation), while zero horizontal gradient of vorticity occurs only for parabolic or logarithmic isopycnals. Therefore the only annulus flow case in which conditions (i)–(iii) all occur together is parabolic isopycnals over parabolic bathymetry, which is our solid body rotation case (§4). Mean flow over any other bathymetry (such as linear bathymetry, as in §5) will necessary violate at least one of (i)–(iii). For uniform azimuthal flow, condition (iii) is satisfied, but the curvature results in non-zero strain rate and non-zero vorticity gradient. Superficially uniform azimuthal flow may appear to be the most similar to uniform rectilinear flow since both cases have isopycnals (linear bathymetry in the present treatment) in the cross-stream direction, but conditions (i)–(iii) identify solid body rotation as the true dynamical analogue of uniform rectilinear flow.

We have verified conditions (i)–(iii) using some additional numerical experiments, whose results are summarized in this paragraph, rather than plotted. The same numerical solver was used in all cases. We considered two cases in which only factor (iii) is violated: (*a*) Uniform straight channel flow (i.e., linear isopycnals) over parabolic bathymetry, and (*b*) solid body rotation (i.e., parabolic isopycnals) over linear bathymetry in an annular channel. Both have zero strain, and therefore were found to be similar to uniform rectilinear flow/solid body rotation in that the magnitudes of their growth rates are very similar, in that the Reynolds stresses work is zero, and in that the results are independent of the barotropic velocity. However, non-zero (though small) growth occurs for $\delta > 1$ in (a) because condition (iii) is violated. We also tested a third case, where only condition (i) is violated: (c) annular flow with logarithmic isopycnals and bathymetry. We found this case to be similar to our uniform azimuthal flow results, though with a more exaggerated dependence on the magnitude of the barotropic velocity $|U_{bt}|$. Unlike uniform azimuthal flow, the logarithmic profile used in case (c) has zero growth rate at $\delta > 1$ because the vorticity is zero.

7. Summary and Discussion

To study the effect of horizontal curvature in flow and bathymetry on baroclinic instability, we study several mean flow and bathymetry cases in an annulus and compare them with uniform mean flow over linear bathymetry in a straight channel (uniform rectilinear flow). We consider uniform rectilinear flow a reasonable though simple test case for deep western boundary currents since these tend to be quite broad relative to the Rossby radius (Xu *et al.* 2015; Stommel & Arons 1972). Some further justification may be required for the use of a periodic annular channel in place of an open domain that is approximately an annular section. We expect that for time intervals short compared to

the travel time of perturbations along the section, azimuthal edge effects will be small, as long as the wavelength is somewhat smaller than the section length.

We find solid body rotation (§4) to be very similar to uniform rectilinear flow, with an exact simple transformation between the dispersion relations of both cases. We trace the similarity in instability properties to the three commonalities between of the mean flows and bathymetries (§6): vanishing strain rate, vanishing vorticity, and constant ratio of bathymetric slope to isopycnal slope $\delta(r) \equiv \delta$. In contrast, the uniform azimuthal flow case (§5), which has (like uniform rectilinear flow) linear isopycnals (and bathymetry), has quite different stability properties from because it has non-vanishing strain rate and mean vorticity. While we began a preliminary exploration of more significantly sheared velocity profiles (i.e., jets and free shear layers), an adequate coverage of this topic requires at least a full additional paper. However, we would like to stress that the analysis in §6 is very general as it is based on the Rayleigh criterion (§3) and on the energy equation (§2.3), and that a few experiments with other simple profiles (§6) support the generality of these results.

Baroclinic instabilities in uniform azimuthal flow differ in several ways from uniform rectilinear flow and solid body rotation: (a) The eigenmodes depend on the mean barotropic velocity. The growth rate of unstable eigenmodes generally decreases with $|U_{bt}|$, unless $\delta \approx 1$. (b) Whereas solid body rotation and uniform rectilinear flow are stable for $\delta \geqslant 1$, uniform azimuthal flow is (weakly) unstable for a small interval of δ greater than 1. That is due to non-zero mean flow vorticity. (c) Negative Reynolds stresses work manifest as part of the barotropic governor effect (BGE). Although BGE is usually attributed to barotropic shear, we find that in non-parallel flow the cause may be generalized to barotropic strain (even when cross-flow shear is zero, as in uniform azimuthal flow). (d) For non zero $|U_{bt}|$, more growing eigenmodes arise, with diverse growth rates, phase speeds, and barotropic to baroclinic energy conversion ratios. (e) Non-normal growth is generally faster and occurs over a larger wavenumber range. The growth rate becomes even larger with increased $|U_{bt}|$ magnitude.

The uniform azimuthal flow case has a small but non-zero growth rate for $\delta > 1$, due to the vorticity associated with curved streamlines, unlike the straight-channel case (Mechoso 1980). Deep western (and some surface) boundary currents often have isopycnal profiles similar to the bathymetric profile, i.e., $\delta(r) \approx 1$ (Xu *et al.* 2015; Stommel & Arons 1972; Stipa 2004*a*; Spall 2010). Thus the increased instability of uniform azimuthal flow relative to uniform rectilinear flow in the $\delta(r) \approx 1$ regime is potentially relevant for the DWBC eddy-shedding observations that motivates this work. Assuming that the DWBC flow is faster in the deeper layer, and that the barotropic flow is in the same direction as the flow in the deeper layer, flow on a convex slope is described (in addition to $\delta \approx 1$) by $U_{bt} < 0$. Negative U_{bt} is indeed the range in which we find the instability is possible for $\delta > 1$ (figure 6, and §3.2). Note that by the symmetry described in §5.3, a concave section would have the same linear growth rates as the convex section described.

The result regarding instability of eigenmodes for $\delta \approx 1$ may also be relevant for parameterizations of eddies on sloping boundaries, still a little explored subject. Isachsen (2011) compares parameterizations based on the extended Eady model with eddy fluxes diagnosed in a Primitive Equation simulation over a straight continental slope. While the parametrization predicts zero flux at $\delta > 1$, the diagnosed eddy flux is very low but non-zero. This might be due to non-zero horizontal vorticity gradients in the flow, which in any case may be relevant to the equivalent parameterization problem on a horizontally curved slope. Non-normal growth, which we found has larger maximal values in uniform azimuthal flow, may also play a role in eddy fluxes when $\delta > 1$, especially since maximal potential non-normal growth rate is independent of the bathymetry. Disturbances with

large non-normal growth, even if they occur rarely, may produce non-zero eddy fluxes for any value of δ.

The curved streamlines and associated strain introduce more growing eigenmodes in uniform azimuthal flow, generally with diminished growth rates and negative Reynolds stresses work. These propagate in various directions and speeds, unlike the strictly topographic Rossby wave-like propagation direction (with shallow water to the right) in uniform rectilinear flow. The wavenumber of maximum growth rate thus changes, and in some cases more than one local maxima in wavenumber exist (for a fixed δ value). This raises questions about the validity for curved slopes of some continental slope eddy parameterizations (Stipa 2004*b*; Isachsen 2011), where diffusivity is determined by solely the global maximum in wavenumber (of the Eady model growth rate).

Perturbations over convex or concave continental slopes have the same perturbation growth rates in uniform azimuthal flow, but the streamfunction profiles are reflected relative to mid-channel on the shallow-deep water axis (§5.3). Uniform azimuthal flow eigenmodes are generally not centered at mid-channel (figure 4). If an eigenmode on a convex slope is centered offshore from mid-channel, the analogous eigenmodes on a concave plane would be displaced shoreward from mid-channel, and vice-versa. While in linear theory this has no direct implications for the growth rate, non-linear evolution, interaction with topography, and bottom boundary layers may result in implications we cannot determine here.

While non-normal peak instantaneous growth rate and the range of unstable wavenumbers are larger due to non-zero mean strain and mean vorticity gradient in uniform azimuthal flow, their importance relative to individual eigenmodes' growth remains unclear due to the transience of non-normal amplification. Differentiating between the two effects would probably require fully non-linear, time-evolution integrations. The domain would preferably be open rather than periodic, to prevent confusion with down and upstream disturbance interaction occurring in finite time. In such a case and especially if the domain were to have changing curvature, it may be that the transience of non-normal growth would not be as large a limitation to actual growth. Non-orthogonality of growing eigenmodes may also influence their nonlinear evolution: their nonzero mutual projections may encourage nonlinear interactions between modes and accelerate the path to finite-amplitude effects.

While we have striven to choose relevant and similar flow profiles for comparison of straight and curved flow and bathymetry, we can imagine a different criterion for selection of the curved profile given a straight flow profile, viz., that the curved profile is the downstream-adjusted profile of the straight flow after meeting a curve in the continental slope. Assume that the upstream (straight flow) boundary current has linear isopycnals and linear bathyemtry, as in uniform rectilinear flow. Once the current traverses a horizontally curved slope section, assuming adjustment to solid-body rotation does not happen, then strain and relative vorticity are necessarily induced in the mean flow (§6). Hence Reynolds stresses will modulate and generally decrease the baroclinic instability growth rates, and the relative vorticity will modulate the range of unstable δ parameters. We find the same results in the uniform azimuthal flow case (§5), which can also be regarded as a study of these effects, when the linear isopycnals remain (cross-stream) approximately linear after meeting the bend in the slope. In §6 we find that a logarithmic isopycnal profile generally has similar results to uniform azimuthal flow, and we expect this to hold quite generally for other broad and relatively uniform flow profiles. Exactly how and how much the mean isopycnal structure actually adjusts to curvature is a question worthy of further investigation.

To summarize, the initial hypothesis is that horizontal curvature of bottom slopes

increases baroclinic instability. We find that to the contrary, peak growth rates are mostly reduced in uniform azimuthal flow relative to uniform rectilinear flow. One exception is the $\delta >\sim 1$ regime. $\delta \sim 1$ is actually quite common in deep boundary currents (Xu *et al.* 2015; Stommel & Arons 1972), and despite the relatively smaller values of growth rates (relative to $\delta < 1$) the increased instability in this regime thus appears relevant. We also find higher peak non-normal growth in uniform azimuthal flow relative to uniform rectilinear flow, but the relative effect of transient non-normal growth versus normal exponential growth is unclear and will remain so unless evaluated in a particular context. The actual profile a deep western boundary current adjusts to (from which baroclinic instability arises), may be different than linear, but it is conjectured above that the results may be quite similar in terms of the baroclinic instability. Exceptions to that may occur, if one takes into account the finite width of the slope and of the current.

AS's and ALS's research was supported by NSF award OCE-1538702. JCM's and AS's research was supported by NSF OCE-1355970. AS would like to thank Mickael D. Chekroun, Yizhak Feliks, and Michael Rudko, for insightful discussions on non-normal growth.

Appendix A. Numerical verification and sensitivity tests

In this appendix we give results of numerical convergence tests, including comparison with some analytical results, to show the validity of the solver and of the numerical solutions. We also give results of sensitivity tests where we vary R_i, R_e, F_1, and F_2, showing that the general results presented in the main text still hold over a larger parameter range.

The numerical setup in a straight-channel was verified in the uniform rectilinear flow case to reproduce the known (Mechoso 1980) analytical dispersion relation. We also verified the numerical solution of the solid body rotation case in a cylinder (annulus with $R_i = 0$) relative to the analytical dispersion relation (4.7). A cylinder (rather than annulus) is chosen because deriving the numerical value of growth rate from the dispersion relation requires first solving the nonlinear algebraic equation (4.4). That can be avoided since in a cylinder since the functions P_m are replaced then by Bessel functions of the first kind J_m, and thereby only (tabulated) Bessel zeros values are needed for the calculation. The results (figure 8a) show a very small relative error in the numerical result with the standard $dr = 0.025$, and decreasing super-exponentially with decreasing dr in the range shown, implying the numerical scheme is convergent.

Since the same solver was used for both solid body rotation and uniform azimuthal flow, the comparison described in the previous paragraph verifies partially the correct setup for uniform azimuthal flow too. We also present in figure 8b the difference in growth rates computed, relative to the result with a higher resolution, namely $dr = 0.003125$. The results suggest that growth rates of all four modes have probably converged to a very good approximation at the resolution used thorough the paper, i.e., $dr = 0.025$. While the specific plot is for $m = 2$, $\delta = -0.2$, and $U_{bt} = 1$, we find that the results are similar in other cases. The difference in the growth rates of the most unstable mode calculated with $dr = 0.025$ relative to that with $dr = 0.0125$ are generally $< 10^{-5}$ inside of the instability boundary.

Further verification for uniform azimuthal flow came from a test of convergence of the uniform azimuthal flow growth rates and frequencies to uniform rectilinear flow values, as the channel inner radius R_i is increased (with constant channel width $W = R_e - R_i$). That is since in the strict $R_i \to \infty$ limit, the mean state of uniform azimuthal flow

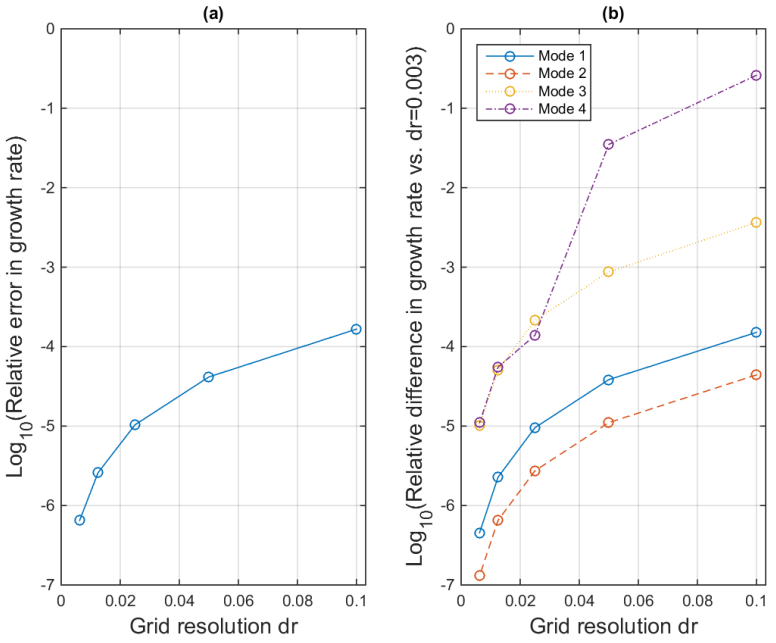

FIGURE 8. (a) Numerical convergence of growth rate for cylinder solid body rotation eigenmodes to that obtained from the analytical dispersion relation (4.7), for azimuthal wavenumber $m = 2$ and bathymetric slope parameter $\delta = 0$. The cylinder width was set by $R_1 = 0$ and $W = R_2 = 7$ to be equivalent to the annulus width taken in sections 4 and 5. The circles denote actual numerical values calculated, in which dr is decreased by factors of two. Note the logarithmic scale of the ordinate. (b) Numerical convergence of uniform azimuthal flow growth rates with various dr values to the value similarly calculated with a twice the highest resolution shown ($dr = 0.00625$), .i.e. with $dr = 0.003125$. Results for all four unstable eigenmodes shown. The presented results are for $m = 2$, $\delta = -0.2$, and $U_{bt} = 1$. The convergence was similarly tested for a large portion of the parameter space. The value actually used to generate all other results in this paper is $dr = 0.025$ (or $dx = 0.025$ in the channel case).

converges to the mean state of uniform rectilinear flow. We verified that for large enough R_i the GR(m, b) functional form for any U_{bt} value indeed became arbitrarily close to the channel result (which is independent of U_{bt}) for large enough R_i values as far as was tested. The convergence test was deemed successful.

The standard experiment described has a radial extent $[R_i, R_e] = [3, 10]$. It is found that moderate increases to domain size (and hence also to current width) do not result in significant changes to the growth rates. For example a current with radial extent $[R_i, R_e] = [3, 15]$ has a similar GR$(\hat{m}, b)$ to the standard experiment considered (with the wavenumber normalized by average domain width, $\hat{m} = mR$). Increasing R_i while keeping channel width constant generally results in more uniform rectilinear flow-like results, as described in the previous paragraph. We find that convergence is slower for larger $|U_{bt}|$ cases, and so the differences described in the main text between annulus and channel instabilities remain qualitatively similar. Decreasing R_i down to a value of 1 (while either keeping $(R_e - R_i)$ constant, or keeping R_e constant) barely changes the growth rates of the fastest growing modes, though the pattern shifts to smaller m's. Note that, as derived in §2.4, $R_i \lesssim 1$ is not consistent with QG.

A layer thickness ratio of 1 ($F_1 = F_2 = 1/2$) was taken throughout the numerical

experiments. Further experiments were done as sensitivity tests with non-equal layers in uniform azimuthal flow, and these show similar growth rate dependence on U_{bt} and m as in the standard experiments, with a few differences. The growth rate maximum is achieved at $F_j = 1/2$ and decreases as $|F_j - 1/2|$ increases. If a line of maximum instability (in m) per δ is fit (in figure 3), then its slope generally increases with H_1/H_2 (maximum $\delta < 0$ instability occurs at higher wavenumbers).

Appendix B. Straight channel equations

We use the uniform rectilinear flow instability case (Pedlosky 1964; Mechoso 1980) as a point of comparison for our investigations. Since it is not new, and to avoid confusing notation, we provide details in this appendix.

Generalizing uniform rectilinear flow by allowing non-uniform currents in a straight channel, we provide below the perturbation modal equations for mean geostrophic along-channel flow $\bar{V}_j = V_j(x)\hat{y}$, and bathymetry $\eta_b(x)$, which vary in the cross channel coordinate (x) only (and in each layer). The background and perturbation streamfunctions are again denoted by $\overline{\psi}_j$ and ψ_j respectively, and therefore $V_j(x) = \partial\overline{\psi}_j/\partial x$. Note that usually the straight channel is modeled with the x coordinate along the channel axis (in the downstream direction). We chose to take the x coordinate in the cross-stream direction for easy comparison with the annular channel, which naturally has the cross-stream coordinate (the radial coordinate r) as the first coordinate of a right-handed triplet.

Assuming an harmonic solution in x and in t, $\psi_j = \mathrm{Re}\{\Psi_j(x)exp(i(ly - \sigma t))\}$ (where Re is the real part of the expression that follows, l is a real down-stream wavenumber, and σ is the complex frequency), we have the (nondimensional) quasi-geostrophic potential vorticity equations (Pedlosky 1964):

$$[V_1 l - \sigma]\left[\frac{\partial^2}{\partial x^2}\Psi_1 - l^2\Psi_1 - F_1(\Psi_1 - \Psi_2)\right] - l\Psi_1\frac{\partial Q_1}{\partial x} = 0, \tag{B 1a}$$

$$[V_2 l - \sigma]\left[\frac{\partial^2}{\partial x^2}\Psi_2 - l^2\Psi_2 - F_2(\Psi_2 - \Psi_1)\right] - l\Psi_2\frac{\partial Q_2}{\partial x} = 0, \tag{B 1b}$$

$$\frac{\partial Q_j}{\partial x} = \frac{\partial^2}{\partial x^2}V_j - F_j\left[(-1)^j\,(V_2 - V_1) - \Delta_{j2}\frac{\partial \eta_b}{\partial x}\right]. \tag{B 1c}$$

For uniform rectilinear flow, $\frac{\partial \eta_b}{\partial x}$ and the V_j are constants. We state the equations in more general form for easy comparison with the general annulus case given in the equation set (2.6). The eigenvalue problem is defined by the PV equations together with no-normal flow boundary conditions. The channel boundaries are denoted by X_i and X_e, and since only their difference (channel width) is important, $X_i = 0$ is chosen. In the standard uniform rectilinear flow experiment, $X_e = 7$, $F_1 = F_2 = 1/2$, and $V_{bt} \equiv (V_1 + V_2)/2 = 0$. The last condition (zero barotropic velocity) is not limiting since the growth rates and eigenmodes are invariant with V_{bt}, which just Doppler-shifts the (real) frequency. The numerical solution is obtained in a similar way as for the annulus.

The eigenmodes streamfunctions are sums of harmonic functions and the nondimen-

sional uniform rectilinear flow dispersion relation is

$$\sigma = V_{bt} + l\frac{K^2\left(F_2 - F_1 - F_2\delta\right) - lF_1F_2\delta + \sqrt{D}}{2K^4 + 2K^2\left(F_1 + F_2\right)}, \tag{B 2a}$$

$$\frac{D}{l^2} = K^8 + \left(2F_2\delta\right)K^6 + \left(-4F_1F_2 + 2F_1F_2\delta + F_2^2\delta^2\right)K^4 + \left(-4F_2^2F_1\delta + 2F_2^2F_1\delta^2\right)K^2 + F_1^2F_2^2\delta^2. \tag{B 2b}$$

Here k, and $K = \sqrt{k^2 + l^2}$ are the cross-stream, and total wavenumbers, respectively. The non-dimensionalization is similar to the uniform azimuthal flow case, and (in non-dimensional variables) $\delta = -\frac{\partial \eta_b}{\partial x}$.

Appendix C. Semicircle theorem

In this section we adapt the Pedlosky (1964) semi-circle theorem, which gives growth-rate bounds and the associated phase-speed bounds to the annular channel, and we extend it for the general case where the bathymetry is not flat. First, we make the transformation $\Psi_j = (U_{j\phi} - cr)b_j$ in equations (3.1a)-(3.1b), then multiply the first and the second equations by $D_1 b_1^*(U_{1\phi} - cr)$ and $D_2 b_2^*(U_{2\phi} - cr)$ respectively. Summing both equations and integrating the result with the volume element (rdr), results, after an integration by parts of the Laplacian terms, in

$$\sum_{n=1}^{2}\int_{R_i}^{R_e}(U_{j\phi} - cr)^2 P_j r dr = D_1D_2\frac{1}{2}\int_{R_i}^{R_e}(U_{1\phi} - U_{2\phi})^2|b_1 - b_2|^2 r dr - D_1\int_{R_i}^{R_e}(U_{2\phi} - cr)J_2\frac{\partial \eta_b}{\partial r}r dr. \tag{C 1}$$

Here we made use of the identity,

$$(U_{1\phi} - cr)(U_{2\phi} - cr) = -\frac{1}{2}\left[(U_{1\phi} - U_{2\phi})^2 - (U_{1\phi} - cr)^2 - (U_{2\phi} - cr)^2\right],$$

with the following definitions:

$$P_j = D_j\left[\left|\frac{\partial}{\partial r}b_j\right|^2 + \frac{m^2 - 1}{r^2}|b_j|^2\right] + D_1D_2\frac{1}{2}|b_1 - b_2|^2$$

$$J_j = D_j|b_j|^2.$$

The real part of (C 1) is thus

$$\sum_{n=1}^{2}\int_{R_i}^{R_e}(U_{j\phi}^2 + c_r^2r^2 - 2U_{j\phi}c_r r - c_i^2r^2)P_j r dr = \frac{1}{2}D_1D_2\int_{R_i}^{R_e}(U_{1\phi} - U_{2\phi})^2|b_1 - b_2|^2 r dr - D_1\int_{R_i}^{R_e}(U_{2\phi} - c_r r)J_2\frac{\partial \eta_b}{\partial r}r dr. \tag{C 2}$$

If $c_i \neq 0$, from the imaginary part of (C 1) we have

$$\int_{R_i}^{R_e}\sum_{n=1}^{2}(U_{j\phi} - c_r r)P_j r^2 dr = -\frac{D_1}{2}\int_{R_i}^{R_e}J_2\frac{\partial \eta_b}{\partial r}r^2 dr. \tag{C 3}$$

TABLE 1. Summary of phase speed bounds

Condition	Phase speed bounds
$\eta_b \equiv 0$	$u_{min} \leqslant c_r \leqslant u_{max}$
$\left(\frac{\partial \eta_b}{\partial r}\right)_{max} < 0$	$u_{min} - \frac{D_1 \left\lvert \left(\frac{\partial \eta_b}{\partial r}\right)_{min} \right\rvert R_e^2}{2R_i(m^2-1)} \leqslant c_r \leqslant u_{max}$
$\left(\frac{\partial \eta_b}{\partial r}\right)_{min} < 0$ and $\left(\frac{\partial \eta_b}{\partial r}\right)_{max} > 0$	$u_{min} - \frac{D_1 \left\lvert \left(\frac{\partial \eta_b}{\partial r}\right)_{min} \right\rvert R_e^2}{2R_i(m^2-1)} \leqslant c_r \leqslant u_{max} + \frac{D_1 \left(\frac{\partial \eta_b}{\partial r}\right)_{max} R_e^2}{2R_i(m^2-1)}$
$\left(\frac{\partial \eta_b}{\partial r}\right)_{min} > 0$	$u_{min} \leqslant c_r \leqslant u_{max} + \frac{D_1 \left(\frac{\partial \eta_b}{\partial r}\right)_{max} R_e^2}{2R_i(m^2-1)}$

For $m > 1$, we can derive the following inequality between integrals of J_j and P_j:

$$\int_{R_i}^{R_e} P_j r^2 dr = D_1 \int_{R_i}^{R_e} \left[\left[\left| \frac{\partial}{\partial r} b_j \right|^2 + \frac{m^2-1}{r^2} |b_j|^2 \right] + D_1 D_2 \frac{1}{2} |b_1 - b_2|^2 \right] r^2 dr$$
$$\geqslant \frac{m^2-1}{R_e^2} D_j \int_{R_i}^{R_e} |b_j|^2 r^2 dr \,,$$

from which follows a result we will refer to as the $J - P$ inequality:

$$\int_{R_i}^{R_e} J_j r^2 dr \leqslant \frac{R_e^2}{m^2-1} \int_{R_i}^{R_e} P_j r^2 dr. \tag{C 4}$$

Pedlosky (1964) found a tighter J-P type inequality for the straight-channel case, using a spectral estimate, which we were unable to adapt to the annulus case. The next two subsections will derive phase speed and growth rate bounds respectively, based on the results so far derived in this section.

C.1. *Bounds on phase speed*

Defining $u_j = U_{j\phi}/r$, equation (C 3) can then be written as

$$\int_{R_i}^{R_e} \sum_{n=1}^{2} (u_j - c_r) P_j r^3 dr = -\frac{D_1}{2} \int_{R_i}^{R_e} J_2 \frac{\partial \eta_b}{\partial r} r^2 dr. \tag{C 5}$$

Bounds on the phase speed can be found from the last equation, using the $J-P$ inequality, assuming that information about Information on η_b and u is available. The bounds are derived separately for 4 different types of η_b profiles, and are summarized in Table 1.

C.2. *Growth rate bound*

We define $u_{\max} = \max_{j=1,2}\{\max_{R_i \leqslant r \leqslant R_e}[u_j(r)]\}$ and $u_{\min} = \min_{j=1,2}\{\min_{R_i \leqslant r \leqslant R_e}[u_j(r)]\}$, and use the following inequality:

$$\begin{aligned} 0 &\leqslant \int_{R_i}^{R_e} \sum_{n=1}^{2} (u_j - u_{\min})(u_{\max} - u_j) P_j r^3 dr \\ &= \int_{R_i}^{R_e} \sum_{n=1}^{2} \left[-u_j^2 + u_j(u_{\max} + u_{\min}) - u_{\min} u_{\max} \right] P_j r^3 dr. \end{aligned} \tag{C 6}$$

In a similar manner to the straight-channel case (Pedlosky 1964), we take (C 6) + (C 2) $-(u_{\min} + u_{\max} - 2c_r)$(C 3), resulting in,

$$\begin{aligned} &\sum_{n=1}^{2} \left[\left(c_r - \frac{u_{\min} + u_{\max}}{2} \right)^2 + c_i^2 - \left(\frac{u_{\max} - u_{\min}}{2} \right)^2 \right] \int_{R_i}^{R_e} P_j r^3 dr \leqslant \\ &- D_1 \int_{R_i}^{R_e} \left(\frac{u_{\max} + u_{\min}}{2} - u_2 \right) J_2 \frac{\partial \eta_b}{\partial r} r^2 dr. \end{aligned} \tag{C 7}$$

Now, using $\left| \frac{2_{max} + u_{min}}{2} - u_j \right| \leqslant \frac{u_{max} - u_{min}}{2}$ together with the J-P inequality (assuming $m > 1$), we obtain the semi-circle inequality:

$$\left(c_r - \frac{u_{\min} + u_{\max}}{2} \right)^2 + c_i^2 \leqslant \left(\frac{u_{\max} - u_{\min}}{2} \right)^2 + \frac{R_e^2 D_1 \left| \frac{\partial \eta_b}{\partial r} \right|_{\max}}{R_i(m^2 - 1)} \left(\frac{u_{\max} - u_{\min}}{2} \right). \tag{C 8}$$

The first term on the left may be dropped as it is positive definite. In fact, by the phase speed bounds derived (in table 1), this term may attain a zero value in all cases.

A tighter bound may be derived by noting that

$$\begin{aligned} &- D_1 \int_{R_i}^{R_e} \left(\frac{u_{\max} + u_{\min}}{2} - u_2 \right) J_2 \frac{\partial \eta_b}{\partial r} r^2 dr \leqslant \\ &- D_1 \min \left[0, \min \left[\left(\frac{u_{\max} + u_{\min}}{2} - u_2 \right) \frac{\partial \eta_b}{\partial r} \right] \right] \int_{R_i}^{R_e} J_2 r^2 dr \,, \end{aligned}$$

from which follows

$$c_i^2 \leqslant \left(\frac{u_{\max} - u_{\min}}{2} \right)^2 - \frac{R_e^2 D_1}{R_i(m^2 - 1)} \min \left[0, \min \left[\left(\frac{u_{\max} + u_{\min}}{2} - u_2 \right) \frac{\partial \eta_b}{\partial r} \right] \right]. \tag{C 9}$$

REFERENCES

Benilov, E. S. 2005 On the stability of oceanic vortices: A solution to the problem? *Dynam. of Atmos. and Oceans* **40** (3), 133–149.

Blumsack, S. L. & Gierasch, P. J. 1972 Mars: The effects of topography on baroclinic instability. *J. Atmos. Sci.* **29** (6), 1081–1089.

Bower, A. S., Armi, L. & Ambar, I. 1997 Lagrangian observations of Meddy formation during a Mediterranean Undercurrent seeding experiment. *J. Phys. Oceanogr.* **27** (12), 2545–2575.

Bower, A. S., Lozier, M. S., Gary, S. F. & Böning, C. W. 2009 Interior pathways of the North Atlantic meridional overturning circulation. *Nature* **459** (7244), 243–247.

Chelton, D. B., Schlax, M. G. & Samelson, R. M. 2011 Global observations of nonlinear mesoscale eddies. *Prog. Oceanogr.* **91** (2), 167–216.

Choboter, P. F. & Swaters, G. E. 2000 On the baroclinic instability of axisymmetric rotating gravity currents with bottom slope. *J. of Fluid Mech.* **408**, 149–177.

Cushman-Roisin, B. 1994 *Introduction to geophysical fluid dynamics*. Prentice Hall.

Dewar, W. K. & Killworth, P. D. 1995 On the stability of oceanic rings. *J. of Phys. Oceanogr.* **25** (6), 1467–1487.

Dong, C., McWilliams, J. C., Liu, Y. & Chen, D. 2014 Global heat and salt transports by eddy movement. *Nat. Commun.* **5**.

Eady, E. T. 1949 Long waves and cyclone waves. *Tellus A* **1** (3).

Farrell, B. F. & Ioannou, P. J. 1996 Generalized stability theory. part i: Autonomous operators. *J. Atmos. Sci.* **53** (14), 2025–2040.

Isachsen, P. E. 2011 Baroclinic instability and eddy tracer transport across sloping bottom topography: How well does a modified Eady model do in primitive equation simulations? *Ocean Modell.* **39** (1), 183–199.

James, I. N. 1987 Suppression of baroclinic instability in horizontally sheared flows. *J. Atmos. Sci.* **44** (24), 3710–3720.

James, I. N. & Gray, L. J. 1986 Concerning the effect of surface drag on the circulation of a baroclinic planetary atmosphere. *Q. J. Roy. Meteorol. Soc.* **112** (474), 1231–1250.

Lavender, K. L, Davis, R. E. & Owens, W. B. 2000 Mid-depth recirculation observed in the interior Labrador and Irminger seas by direct velocity measurements. *Nature* **407** (6800), 66–69.

Lavender, K. L., Owens, W. B. & Davis, R. E. 2005 The mid-depth circulation of the subpolar North Atlantic ocean as measured by subsurface floats. *Deep Sea Res. Part I* **52** (5), 767–785.

McDowell, S. E. & Rossby, H. T. 1978 Mediterranean water: An intense mesoscale eddy off the Bahamas. *Science* **202** (4372), 1085–1087.

McWilliams, J. C. 1985 Submesoscale, coherent vortices in the ocean. *Rev. Geophys.* **23** (2), 165–182.

McWilliams, J. C. 2008 The nature and consequences of oceanic eddies. In *Ocean modeling in an eddying regime* (ed. M. W. Hecht & H. Hasumi), chap. 1. John Wiley and Sons.

Mechoso, C. R. 1980 Baroclinic instability of flows along sloping boundaries. *J. Atmos. Sci.* **37** (6), 1393–1399.

Molemaker, M. J., McWilliams, J. C. & Dewar, W. K. 2015 Submesoscale instability and generation of mesoscale anticyclones near a separation of the California Undercurrent. *J. Phys. Oceanogr.* **45** (3), 613–629.

Moler, C. B. & Stewart, G. W. 1973 An algorithm for generalized matrix eigenvalue problems. *SIAM J. on Numer. Analysis* **10** (2), 241–256.

Mysak, L. A. & Schott, F. 1977 Evidence for baroclinic instability of the Norwegian Current. *J. Geophys. Res.* **82** (15), 2087–2095.

Olson, D. B 1991 Rings in the ocean. *Ann. Rev. of Earth and Plan. Sci.* **19**, 283.

Paldor, N. & Nof, D. 1990 Linear instability of an anticyclonic vortex in a two-layer ocean. *J. of Geophy. Res.: Oceans* **95** (C10), 18075–18079.

Pedlosky, J. 1964 The stability of currents in the atmosphere and the ocean: Part I. *J. Atmos. Sci.* **21** (2), 201–219.

Pedlosky, J. 1970 Flow in rotating stratified systems. *Notes on the 1970 Summer Study Program in GFD at WHOI* pp. 1–68, https://darchive.mblwhoilibrary.org/handle/1912/3000.

Pedlosky, J. 1987 *Geophysical fluid dynamics*. Springer Science and Business Media.

Phillips, N. A. 1951 A simple three-dimensional model for the study of large-scale extratropical flow patterns. *J. Meteor.* **8** (6), 381–394.

Pichevin, T. 1998 Baroclinic instability in a three layer flow: a wave approach. *Dynam. Atmos. Ocean* **28** (3), 179–204.

Poulin, F. J., Stegner, A., Hernández-Arencibia, M., Marrero-Díaz, A. & Sangrà, P. 2014 Steep shelf stabilization of the coastal Bransfield Current: Linear stability analysis. *J. Phys. Oceanogr.* **44** (2), 714–732.

Rayleigh, Lord 1880 On the stability, or instability, of certain fluid motions. *Proc. London Math. Soc.* **11**, 57–70.

Sherwin, T. J., Williams, M. O., Turrell, W. R., Hughes, S. L. & Miller, P. I. 2006 A description and analysis of mesoscale variability in the färoe-shetland channel. *J. Geophys. Res. Oceans* **111** (C3).

Smith, P. C. 1976 Baroclinic instability in the Denmark Strait overflow. *J. Phys. Oceanogr.* **6** (3), 355–371.

Spall, M. A. 2010 Non-local topographic influences on deep convection: An idealized model for the Nordic Seas. *Ocean Modell.* **32** (1), 72–85.

Stegmann, P. M. & Schwing, F. 2007 Demographics of mesoscale eddies in the California Current. *Geophys. Res. Lett.* **34** (14).

Stern, A., Nadeau, L. & Holland, D. 2015 Instability and mixing of zonal jets along an idealized continental shelf break. *J. Phys. Oceanogr.* **45** (9), 2315–2338.

Stewart, A. L., Dellar, P. J. & Johnson, E. R. 2011 Numerical simulation of wave propagation along a discontinuity in depth in a rotating annulus. *Computers & Fluids* **46**, 442–447.

Stewart, A. L., Dellar, P. J. & Johnson, E. R. 2014 Large-amplitude coastal shelf waves. In *Modeling Atmospheric and Oceanic Flows* (ed. T. von Larcher & P. D. Williams), pp. 229–253. Hoboken, NJ: Wiley.

Stipa, T. 2004*a* Baroclinic adjustment in the Finnish coastal current. *Tellus A* **56** (1), 79–87.

Stipa, T. 2004*b* On the sensitivity of coastal quasigeostrophic edge wave interaction to bottom boundary characteristics: possible implications for eddy parameterizations. *arXiv preprint physics/0401119* .

Stommel, H. & Arons, A. B. 1972 On the abyssal circulation of the world oceanV. The influence of bottom slope on the broadening of inertial boundary currents **19** (10), 707–718.

Trefethen, L. N., Trefethen, A. E., Reddy, S. C. & Driscoll, T. A. 1993 Hydrodynamic stability without eigenvalues. *Science* **261** (5121), 578–584.

Williams, P. D., Read, P. L. & Haine, T. W. N. 2010 Testing the limits of quasi-geostrophic theory: application to observed laboratory flows outside the quasi-geostrophic regime. *J. Fluid Mech.* **649**, 187–203.

Xu, X., Rhines, P. B., Chassignet, E. P. & Schmitz Jr, W. J. 2015 Spreading of Denmark Strait Overflow Water in the western subpolar North Atlantic: insights from eddy-resolving simulations with a passive tracer. *J. Phys. Oceanogr.* **45** (2015), 2913–2932.